

---

# IRES REPORT

## Pulsar Mode Change Detection

---

August 20, 2019

Min Young Kim  
University of Washington Seattle  
Advisor: Bhal Chandra Joshi

# Contents

0.1	Overview . . . . .	3
0.2	Pulsars . . . . .	4
0.3	Radio Astronomy . . . . .	5
0.4	J0332+5434 . . . . .	6
0.5	Data Preparation . . . . .	7
0.6	Gaussian Fitting . . . . .	11
0.7	Kolmogorov-Smirnov Test . . . . .	12
0.7.1	Discrete KS Test . . . . .	12
0.7.2	Application to J0332+5434 . . . . .	13
0.8	Wavelet Analysis . . . . .	17
0.8.1	Continuous Wavelet Transform . . . . .	17
0.8.2	Haar wavelet . . . . .	18
0.8.3	Other Wavelet Examples . . . . .	20
0.8.4	Discrete Haar Transform . . . . .	23
0.8.5	Discrete Wavelet Transform . . . . .	27
0.8.6	Wavelet Power Spectrum . . . . .	30
0.9	Wavelet Significance Testing . . . . .	33
0.9.1	Pointwise Testing . . . . .	33
0.9.2	Areawise Testing . . . . .	35
0.9.3	Geometric Testing . . . . .	36
0.9.4	Cumulative Areawise Testing . . . . .	37
0.9.5	Other Significance Tests . . . . .	40
0.10	Application to J0332+5434 . . . . .	43
0.10.1	Ratio of Profiles . . . . .	44
0.10.2	Difference of Profiles . . . . .	44
0.11	Test Comparisons . . . . .	57
0.12	Additional Resources . . . . .	59

0.13 References . . . . .	60
---------------------------	----

\*All plots are original unless it says "Take from ..."

\*Equations are based off of notes I took, so might be identical to sources

## 0.1 OVERVIEW

The goal of this project was to identify changes in the shape of pulse profiles, known as mode changes. Three methods were tested: Gaussian fitting, Kolmogorov-Smirnov (KS) test, and wavelet analysis (cumulative areawise testing) on the difference and ratio of profiles.

The test results were compared against 12 out of 61 visually classified mode changes, where we considered the decrease in *only* the 3rd peak of profile as a mode change. This made it difficult to verify the accuracy of a test.

KS test identified 3 abnormal profiles, one of them which matched a visually classified profile. The other two seem to be identifying a change in the central peak, something we didn't consider as a mode change when visually classifying.

Wavelet analysis on ratio and difference of profiles was uninformative, as many had patches in its spectrum. However, we know that holes in a patch indicate a significant feature. If we apply this extra filter on the difference spectra, we identify 11 profiles as significant, 7 of which correctly identify visually classified mode change. 4 spectra almost formed holes, and one of them identify an eighth profile from the visually classified profiles. Reasons as to why the extra condition of holes turn a completely uninformative test result to one that has a success rate greater than 50% is not clear, though some potential sources are identified.

To properly assess the validity of the KS test and wavelet significance test, we need to (1) expand our definition of mode change used when visually identifying mode changes, or (2) possibly not even do a visual test but use a method widely accepted in literature, and (3) use a larger dataset.

Some common acronyms used in this report are

**WN** : White Noise    **CWT** : Continuous Wavelet Transform    **DWT** : Discrete Wavelet Transform    **DHT** : Discrete Haar Transform    **KS test** : Kolmogorov-Smirnov test    **CDF** : Cumulative Distribution Function

## 0.2 PULSARS

Pulsars are the remnants of a star that has gone supernova at the end of its life cycle. It leaves behind an extremely dense neutron star, with strong gravitational and magnetic fields. The rotational axis and magnetic axis are not necessarily aligned. Electron flow along the magnetic field lines at the polar cap is a source of radio emission. This radio signal is distributed over a range of radio frequencies, and it is thought that higher frequency signals are typically generated closer to the surface of the pulsar, in what is known as radius-to-frequency mapping.

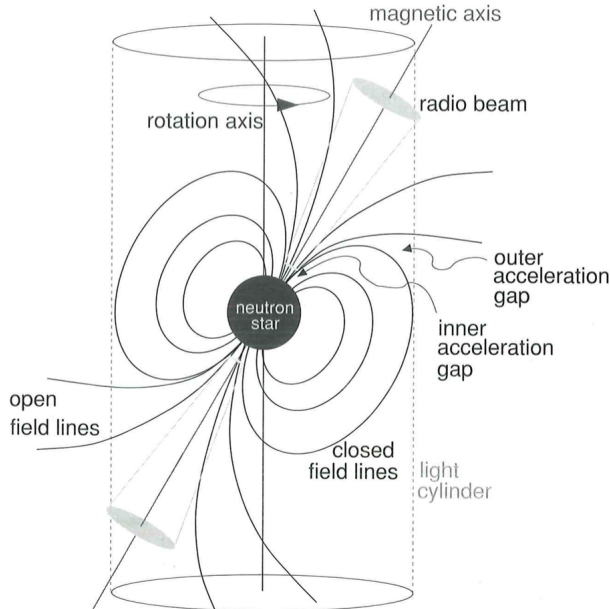


**Figure 1:** A simplified pulsar model. Taken from [12]

Pulsar signals are extremely faint, so a commonly used unit of flux density is the Jansky.  $1\text{Jy} = 10^{-26} \text{W m}^{-2} \text{Hz}^{-1}$ . The median flux density for pulsars is around 0.8mJy [12]. Hence, a technique called folding is employed to obtain an average pulsar profile. One first identifies the period of the pulsar in the Fourier frequency domain. Then, given a continuous "time series" of pulsar signals, one cuts the data into chunks of length equal to the pulsar period, and sums them up together. Because random Gaussian noise/white noise (WN) has a zero mean, for  $N$  folds of data chunks, the signal increases proportional to  $N$ , while WN increase proportional to  $\sqrt{N}$ . The end result is an average pulsar profile with a much higher signal to noise ratio (SNR). A more detailed guide to folding can be found in section 7.1 of Handbook of Pulsar Astronomy [12].

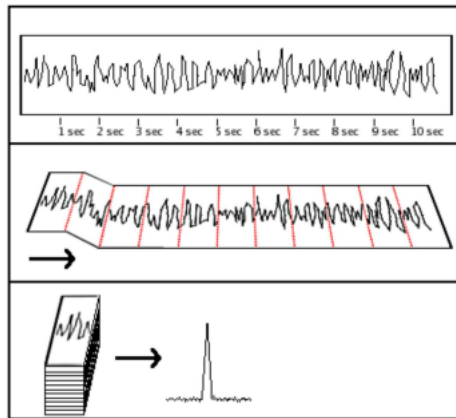
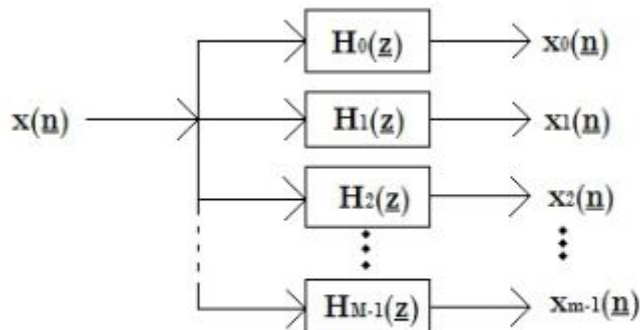


**Figure 2:** Folding of a pulsar signal to increase SNR. Taken from [12]

### 0.3 RADIO ASTRONOMY

How are these signals detected? The most basic method is the use of a filter bank to detect radio signals over a range of radio frequencies [3]. A filter bank has a large number of narrow band filters, dividing a range of frequencies into discrete bins. Each band filter ideally only measures flux corresponding to its own observing frequency. Thus, a telescope receiver is able to measure radio signals at various frequencies.



Multidimensional Analysis Filter Banks

**Figure 3:** A diagram of a filter bank.

Radio telescope dishes generally have a paraboloid shape [3]. Pulsar signals are so far away that they can be approximated as plane waves, and when such plane waves encounter a paraboloid reflector, the waves are focused at the focal spot of the dish. The cross section of the wave power at the focal point is not a point, but produces a

single slit interference pattern. The width of the focal spot is typical  $\frac{F\lambda}{D}$ , where  $F$  is the focal length,  $\lambda$  is the wavelength, and  $D$  is the diameter of the aperture. Thus, increasing the diameter of the aperture decreases the focal spot width and increases resolution. This leads to the idea of a number of radio telescopes distributed over a large area, effectively increasing its diameter. At the Giant Meter Radio Telescope (GMRT) in India, 30 radio telescopes are distributed in a Y shape, giving an effective total aperture diameter of a 25km [15]. Unlike the Greenbank telescope in West Virginia, which has 2000 metal reflectors which are motor controlled to compensate for deformations due to wind, gravity, and temperature, GMRT uses a wire mesh with varying grid densities as a function of radius of the dish. The varying densities of the mesh correspond to different frequency bands. The use of wire mesh also means a reduced gravitational stress on the telescope.

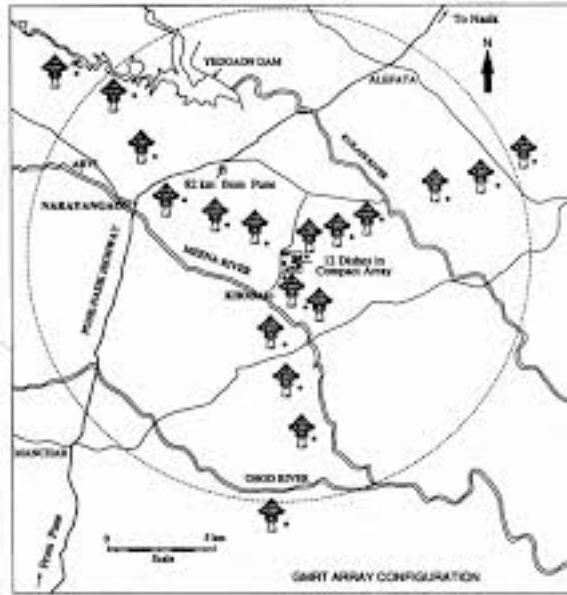


**Figure 4:** Giant Meter Radio Telescope in India. Taken from [15]

## 0.4 J0332+5434

The goal of the project is to detect and characterize mode changing phenomenon of pulsars. Mode changing is a phenomenon in which a pulsar average profile changes for some time into its abnormal mode, then reverts back to its normal mode. Typically, a pulsar spends majority of its time in its normal mode. Mode changing was first observed in B1937+21. The pulsar whose data was used in this report, J0332+3435, is

a pulsar with a period of .714 seconds, and a dispersion measure of  $26.76 \text{ cm}^3 \text{ pc}^{-1}$  [2]. It is one of the brightest pulsars in the northern hemisphere, and its high SNR makes it ideal to test different mode detection methods on. Its normal mode consists primarily of 3 peaks, the central being the tallest. It's abnormal mode primarily features a decrease in amplitude of the third peak.

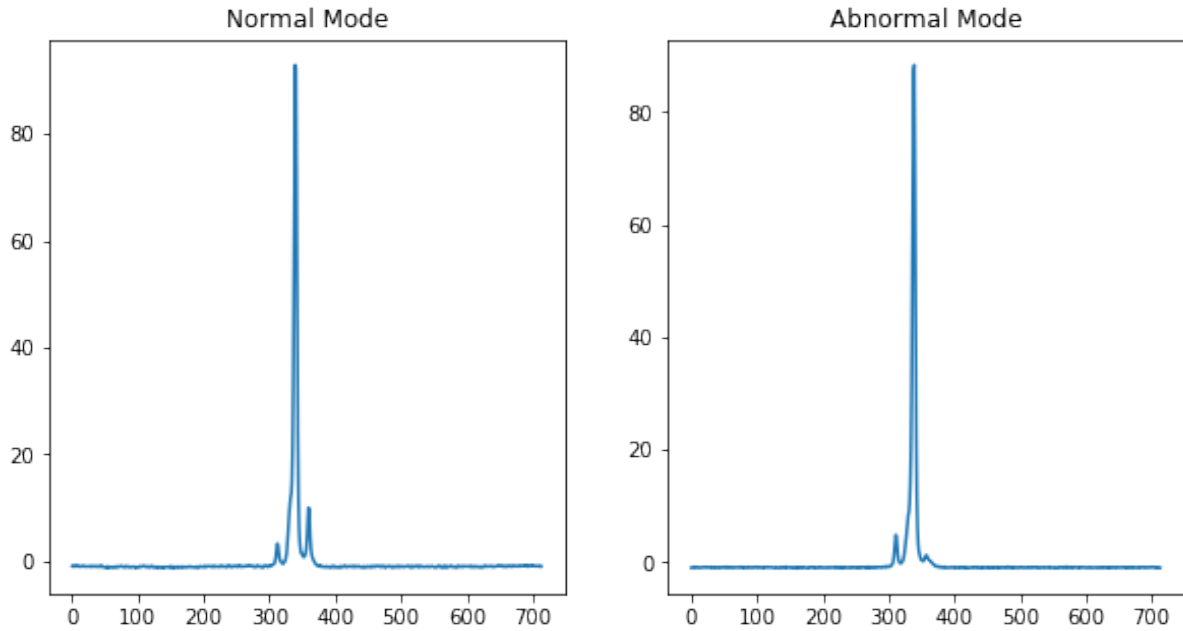


**Figure 5:** Pulse profiles of J0332+5434. There is a clear change in profile shape, specifically the decrease in amplitude of the third peak.

The data used was gathered from Ooty telescope in South India. After discarding noisy data which did not show any pulsar signals, there remained 62 average profiles to work with. Each profile had 1250 pulses folded. The profiles had varying amounts of white noise. Each profile had a length of 714 bins, corresponding to the pulsar period of .714 seconds. Hence, the sampling period was 1ms.

## 0.5 DATA PREPARATION

First, the profiles needed to be aligned in phase. While one can arbitrarily choose a standard profile to align the remaining 61 profiles to, it is crucial to choose the standard profile to have its peaks occur near the center of the profile. The reason is explained in Section 0.7.2. This aligning of phase is done in the Fourier frequency domain, with the

use of Fourier Shift Theorem. The following equations are from [19].

First, the Discrete Fourier Transform (DFT) of a signal  $x$  is defined as

$$X(\omega_k) \equiv \sum_{n=0}^{N-1} x(t_n) e^{-i\omega_k t_n}, \quad k = 0, 1, 2, \dots, N-1$$

where

$x(t_n)$   $\equiv$  input signal amplitude at time  $t_n$ ,

$T$   $\equiv$  sampling interval,

$t_n \equiv nT$  =  $n^{\text{th}}$  sampling instant,  $n \in \mathbb{N}$ ,

$X(\omega_k)$   $\equiv$  spectrum of  $x$  at frequency  $\omega_k$ ,

$\omega_k \equiv k\Omega = \frac{k2\pi f_s}{N} = \frac{k2\pi}{NT}$  =  $k^{\text{th}}$  frequency sample,

$\Omega \equiv \frac{2\pi}{NT}$  = radian frequency sampling interval,

$f_s \equiv \frac{1}{T}$  = sampling rate ( $\frac{\text{samples}}{\text{time unit}}$ , Hz if seconds), and

$N$  = number of time/frequency samples.

Likewise, the Inverse DFT is defined by

$$x(n) = \frac{1}{N} \sum_{k=0}^{N-1} X(k) e^{i2\pi nk/N}, \quad n = 0, 1, 2, \dots, N-1$$

The Fourier Shift Theorem states,

$$x(n - \Delta) \leftrightarrow e^{-i\omega\Delta} X(\omega_k)$$

where  $\omega_k \equiv \frac{2\pi k}{N}$ ,  $k = 0, 1, 2, \dots, N-1$ ,

and the signal in time  $x(n)$  is delayed by  $\Delta$  samples, hence  $\Delta \in \mathbb{Z}$ .

In words, the Fourier Shift theorem can be interpreted as such: a shift in time domain by  $\Delta$  corresponds to a multiplication by a linear phase term  $e^{-i\omega_k\Delta}$  in the Fourier domain. Hence, given the profile data, one can calculate the time delay  $\Delta$  in units of samples/bins against some reference profile, apply DFT to the profile, multiply by the linear phase factor  $e^{-i\omega_k\Delta}$ , and then take the inverse DFT. The end result should be a profile that is now aligned with some reference profile in phase.

How does one calculate  $\Delta$ ? Ideally, one would apply a root-finding algorithm known as Brent's method to equations (A 7) and (A 8) in [21] solve for  $\tau$  and convert it to number

of samples. However, due to the high SNR of J0332+5434 data, it was enough to simply calculate  $\Delta$  by taking the difference in number of samples between two given profiles' maximum amplitude. For other pulsar profiles with a lower SNR, or a profile shape that doesn't have a single extreme peak, it would be best to implement Brent's method.

After aligning all the profiles against some reference profile, one needs to calibrate and normalize each profile. Calibration is done by subtracting the mean of each profile from itself. Normalization is done simply by dividing each profile by its integrated area.

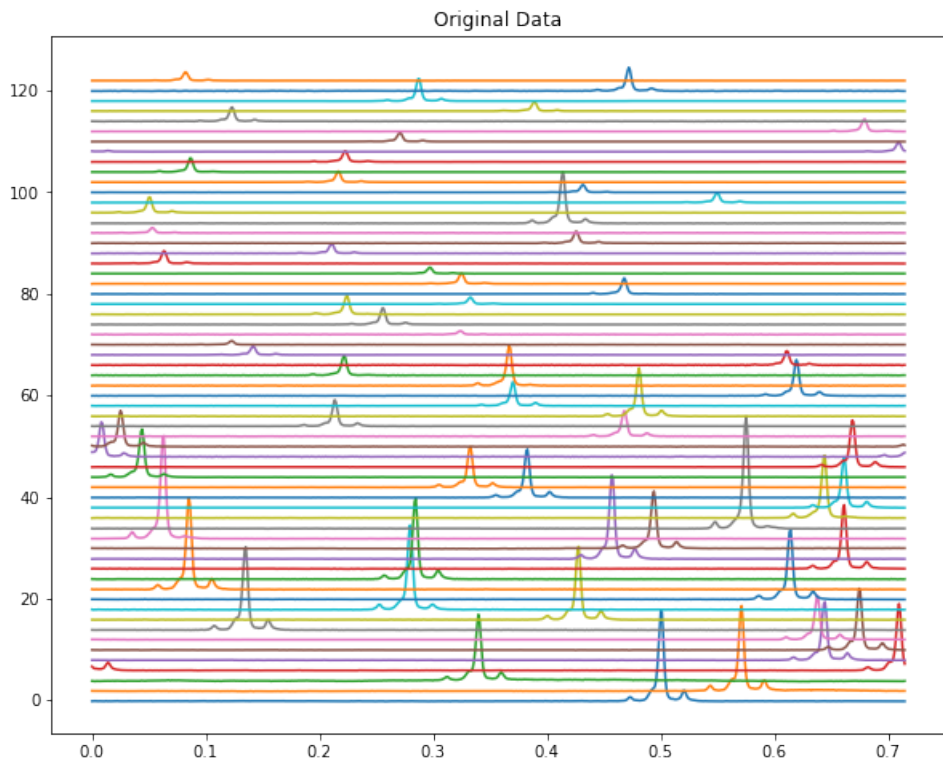


**Figure 6:** Original data of 62 profiles.

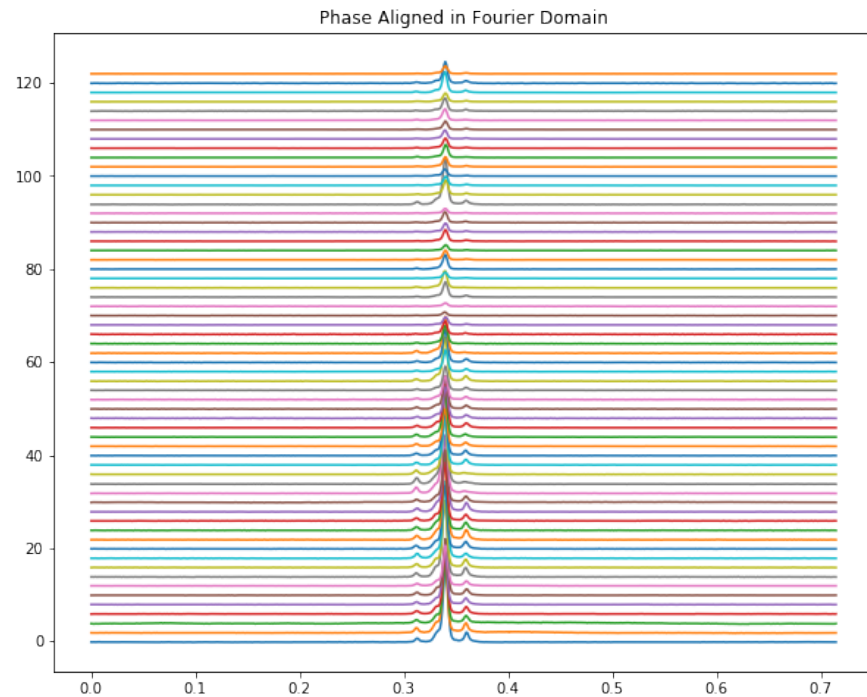


**Figure 7:** Phase aligned in Fourier domain.

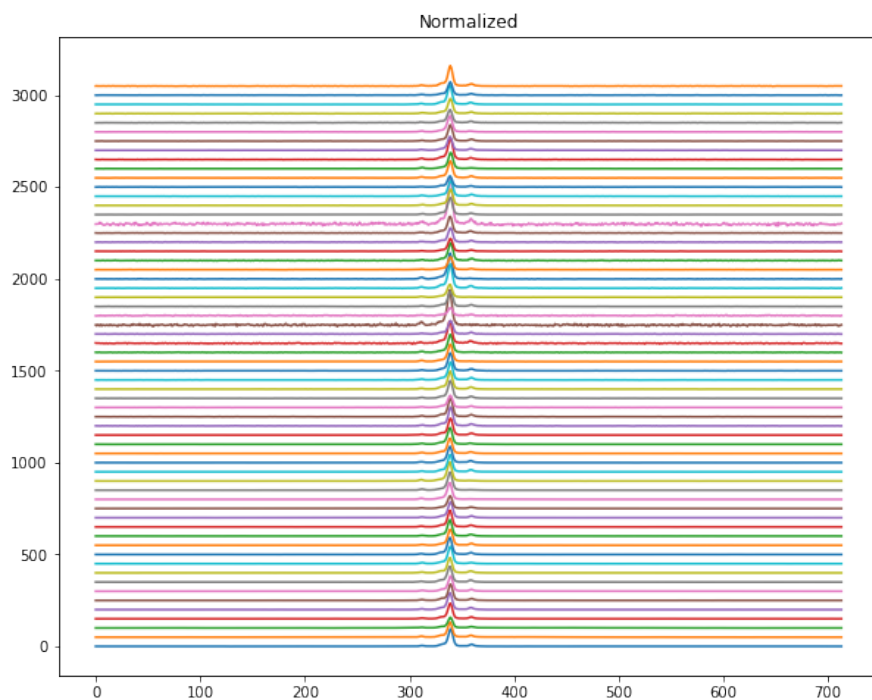


**Figure 8:** Finally, normalized profiles to 1.

## 0.6 GAUSSIAN FITTING

One of the most basic methods is Gaussian fitting. One models a profile as a sum of Gaussian components, then for each profile produce a Gaussian fit. By observing how the amplitude of the fits vary over epoch, one can detect mode changes.

The Gaussian model used contained five components. They were produced simply using the Gaussian probability density function

$$g(x) = \frac{1}{\sqrt{2\pi\sigma^2}} e^{-\frac{1}{2}(\frac{x-\mu}{\sigma})^2}$$

where  $\sigma$  is the standard deviation,  $\mu$  is the mean. It does take some trial and error to get correct parameters for the Gaussian components, as a single model might not adequately fit all the profiles.

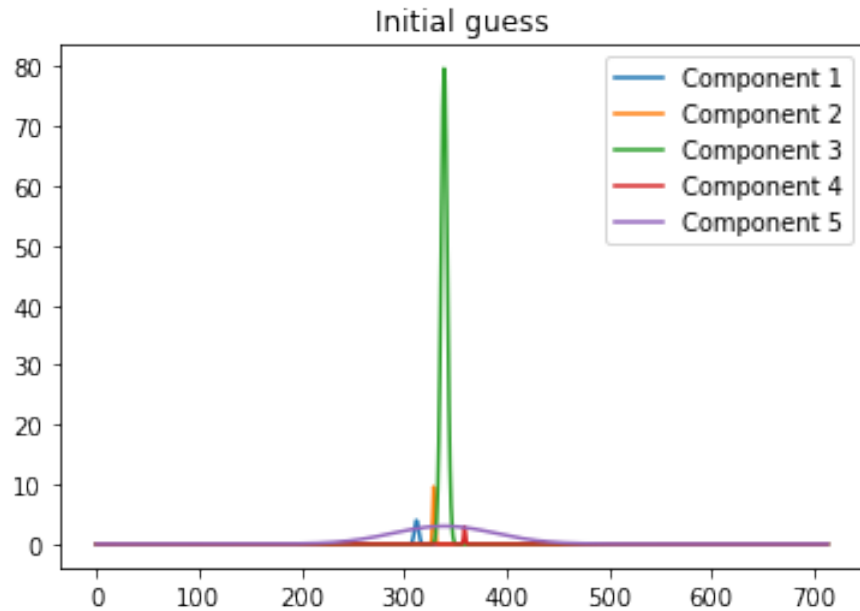


**Figure 9:** Initial guess of five Gaussian components.

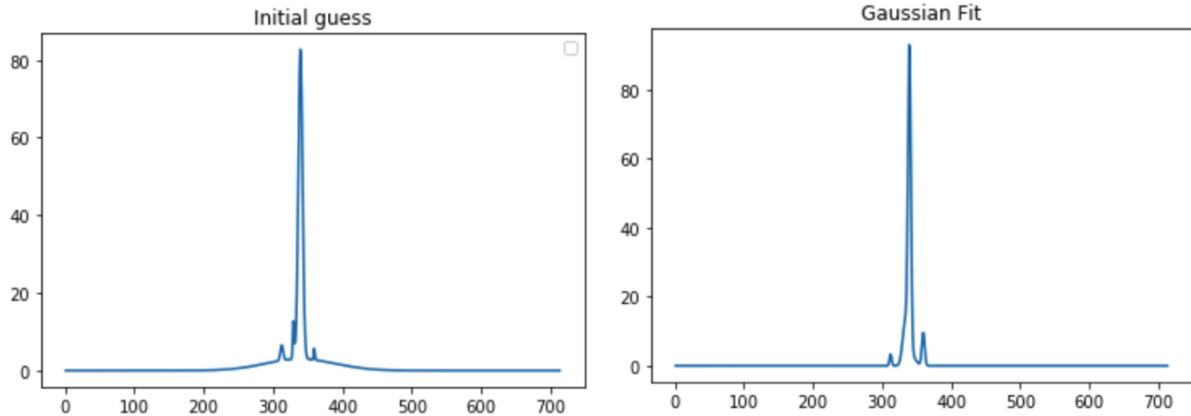


**Figure 10:** Gaussian model pre and post fit

## 0.7 KOLMOGOROV-SMIRNOV TEST

### 0.7.1 Discrete KS Test

The Kolmogorov-Smirnov (KS) test is a non-parametric, goodness-of-fit test [22]. A one-sample KS test attempts to determine if a set of observed values are generated from some reference distribution. A two-sample KS test attempts to determine if two observed data sets come from the same distribution. In this project, we use a one-sample KS test. A continuous, one-sample KS test is defined as follows [22].

Let  $F_0(x)$  be the hypothesized distribution,  $F_{data}(x)$  be the empirical distribution of observed data. The test statistic used is

$$D = \sup_x |F_0(x) - F_{data}(x)|$$

where  $\sup_x$  denotes the supremum over all  $x$ . Once one obtains the D-statistic, one can calculate the corresponding p-value. The p-value is the probability of observing the given data under the assumption that  $H_0$ , the null hypothesis, is true. In this context,  $H_0$  would be that  $F_{data}(x)$  is sampled from the hypothesized distribution  $F_0(x)$ . The alternative hypothesis,  $H_\alpha$ , would be that given data does not come from the hypothesized distribution. Given some significance level  $\alpha$ , say  $\alpha = .05$ , if the p-value  $< \alpha$ , then we would reject  $H_0$  and favor  $H_\alpha$ . Note that failure to reject  $H_0$  does not

necessarily imply the data is drawn from the null distribution. It simply means there was not enough evidence to reject the  $H_0$ .

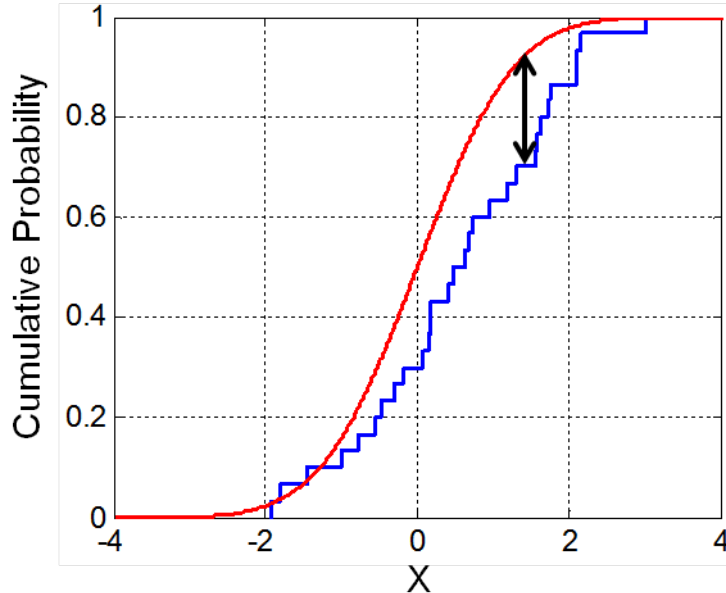


**Figure 11:** A one sample continuous KS test. Hypothetical CDF in red, empirical CDF in blue. The arrow denotes the D statistic at the given point. Taken from [11].

### 0.7.2 Application to J0332+5434

First, we picked a reference profile, whose cumulative distribution function (CDF) will serve as our null distribution. The very first profile was chosen arbitrarily. Note that a KS test is more sensitive to deviations near the center of the distribution. This is why when phase aligning in the data preparation step, it was necessary to align all profiles such that the pulse signals occurred near the center. Once we have picked our null distribution, we simulate 1000 profiles by adding WN on top of the reference profile. Then, performing the KS test on the 1000 simulated profiles' CDF against the reference profile's CDF returns 1000 D-statistics, whose distribution is shown in Figure 14. If we desire a significance level  $\alpha_{ks}$  when performing the KS test on the real profiles, the critical D-statistic,  $D_{crit}$ , corresponding to  $\alpha_{ks}$  is the  $1 - \alpha_{ks}$  th percentile of the simulated distribution. A significance level of  $\alpha_{ks} = .05$  was used.

Next, we perform the KS test on the remaining 61 profiles CDFs against the null CDF, and obtain D-statistics. The distribution of the D-statistics are shown in Figure 14. If a

given profile's D-statistic is larger than  $D_{crit}$ , then we conclude that that profile is significant at the  $\alpha_{ks}$  level, and hence displays a mode different from that of the reference profile. The KS test classified 3 profiles as significant, and only one of them matched the 12 visually classified abnormal profiles. However, the other two seemed to identify a mode change concerning the central peak. Our consideration of only the decrease in 3rd peak as a mode change when visually classifying profiles seems to cause an issue when trying to assess the accuracy of a test result.

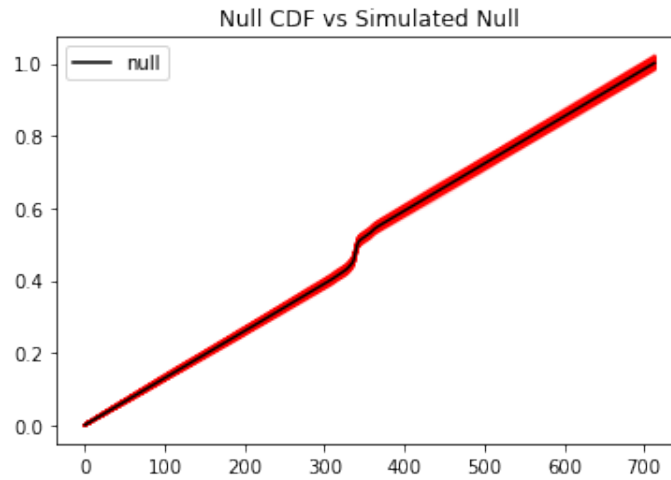


**Figure 12:** CDF of the null profile in black. CDFs of 1000 WN simulations in red.

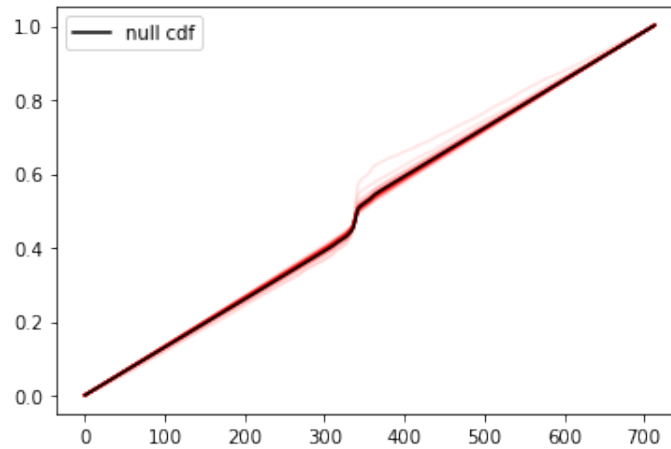


**Figure 13:** CDF of the null profile in black. CDFs of other 61 profiles in red.

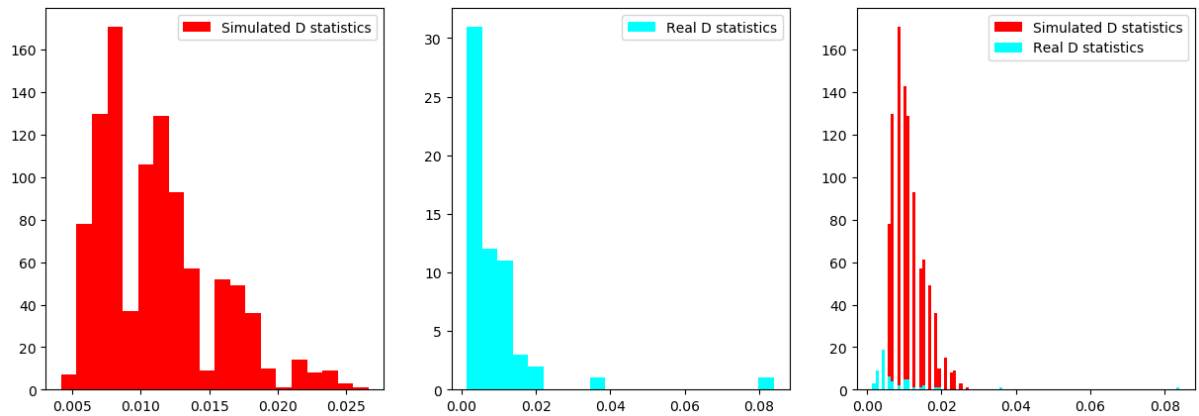


**Figure 14:** Distributions of D-statistics from (a) 1000 simulations (b) 61 profiles (c) the two distributions over plotted.

One can then plot the mode changes as a function of epoch to potentially identify a characteristic period of mode changes.

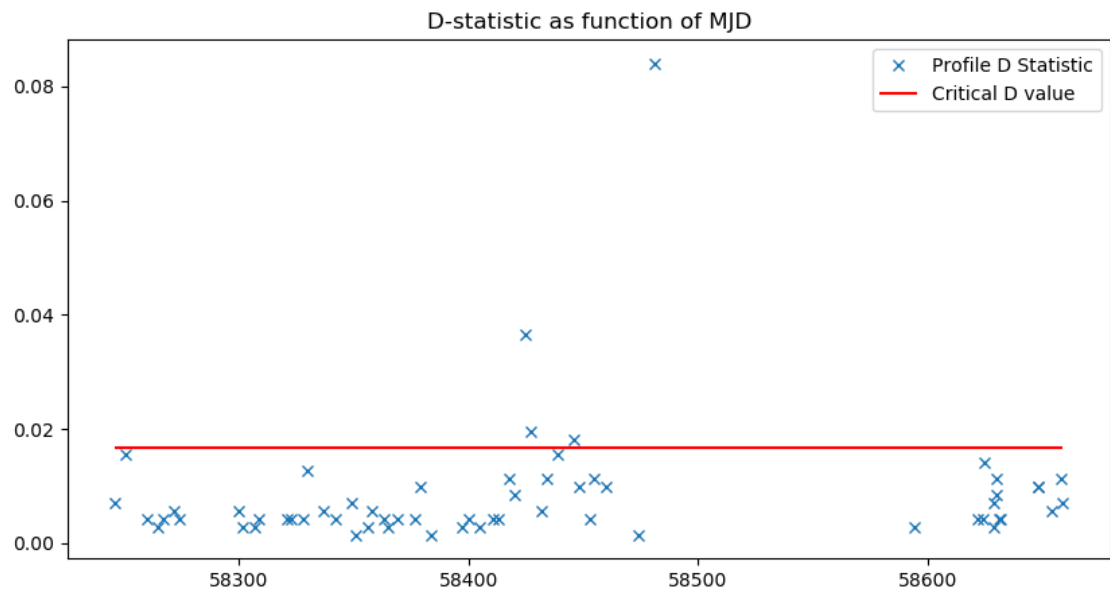


**Figure 15:** D-statistics of profiles plotted as a function of epoch. Red line indicates  $D_{crit}$ . Profiles with D-statistics above this line is significant at  $\alpha_{ks} = .05$ .

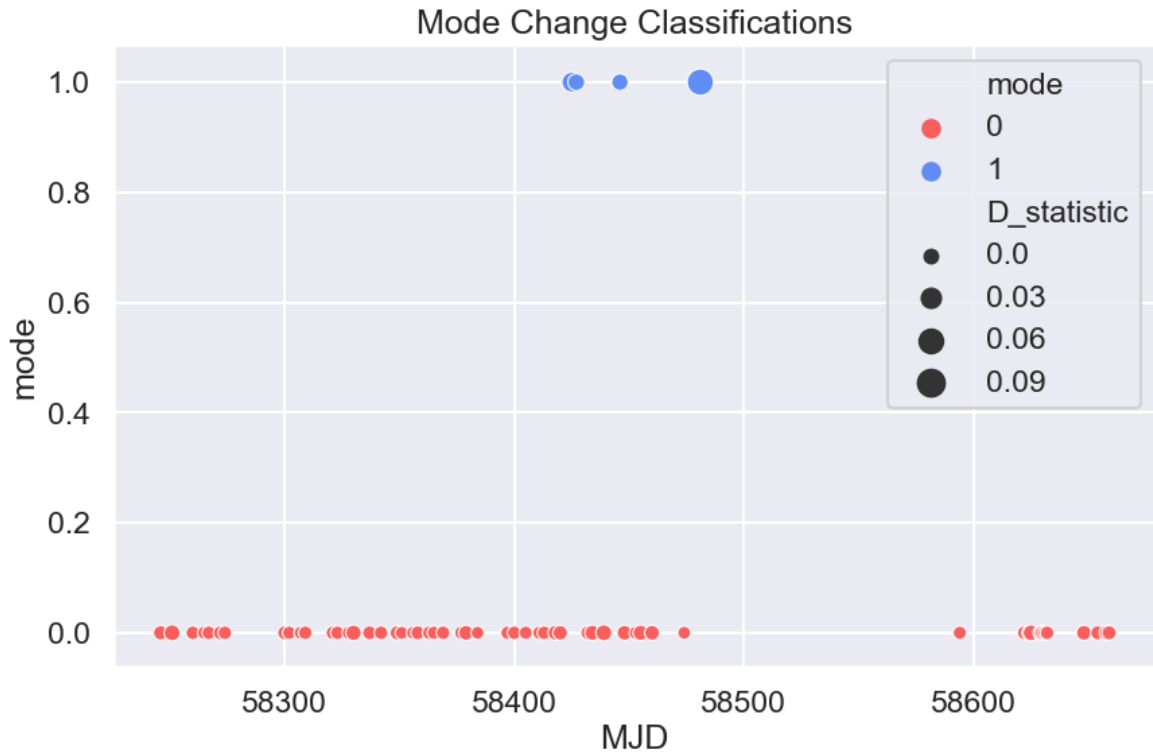


**Figure 16:** Plotting mode changes as a function of epoch. 0 indicates same mode as reference profile. 1 indicates a different mode. Size of marker indicates D-statistic value.

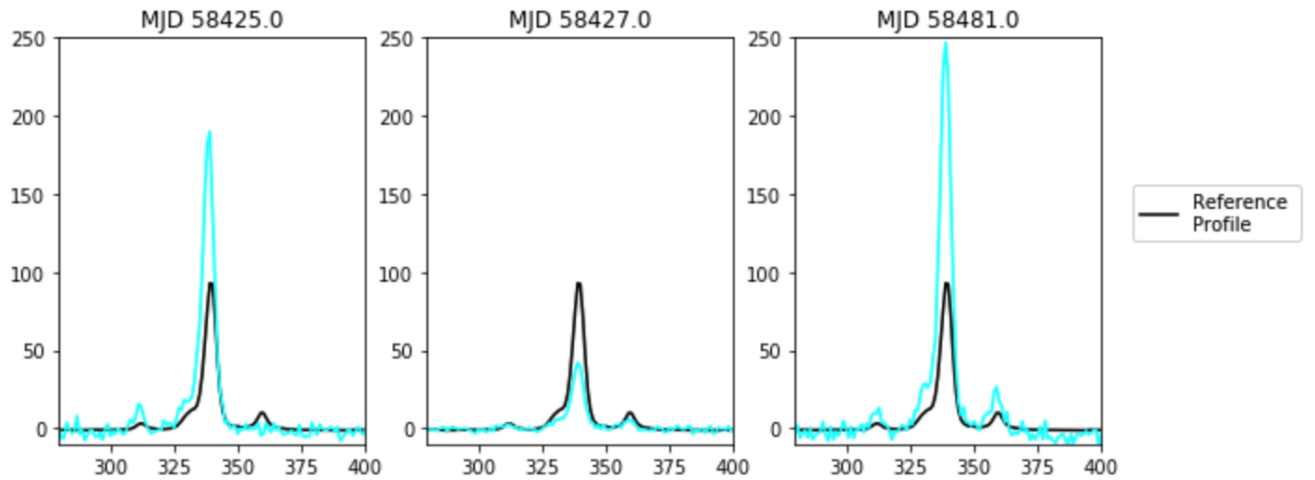


**Figure 17:** The three profiles identified by KS test as significant, plotted against reference profile in black.

## 0.8 WAVELET ANALYSIS

The Fourier transform is a common tool for analyzing signals. However, its downside is that one can have information about a signals frequency content or time content (as a time series), but not both. There are workarounds around this, such as the windowed Fourier Transform, but it still has its disadvantages. This motivates the use of a wavelet transform, which compromises between time and frequency content to obtain both. At higher frequencies, we achieve a precise time localization at the expense of frequency localization. At lower frequencies, we achieve a precise frequency localization at the expense of time localization. A popular visualization commonly used is Figure 18. In the following subsections, equations are taken from notes I made by reading An Introduction to Wavelet Analysis by Walnut [24] and Ten Lectures on Wavelets by Debauchies [6].

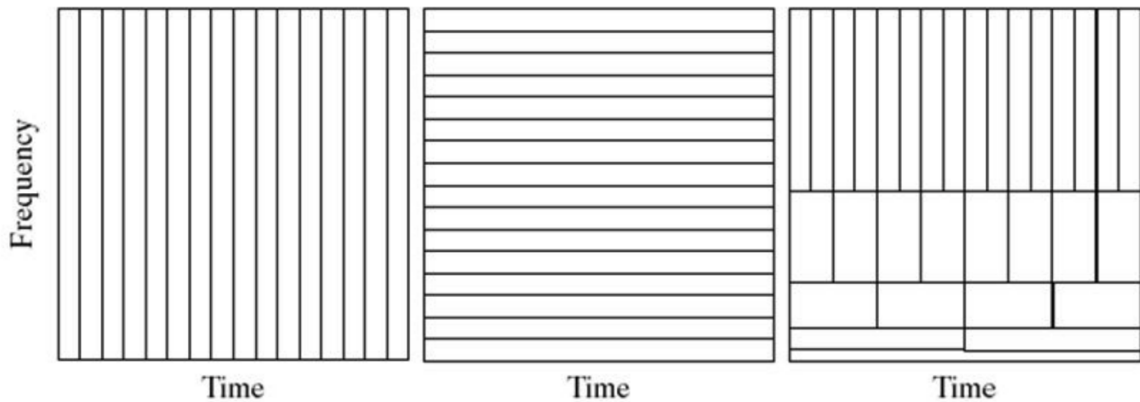


**Figure 18:** In the time-frequency plane, (a) Time series (b) Fourier transform (c) Wavelet Transform. Taken from [9].

### 0.8.1 Continuous Wavelet Transform

In wavelet analysis, wavelets are functions of two parameters, a translation parameter  $b$  and a dilation parameter  $a$ , both of which vary continuously over  $\mathbb{R}$  ( $a \neq 0$ ). We define  $\psi$ , the "mother" wavelet. Then, its family of "daughter" wavelets is defined as

$$\psi^{a,b}(x) = \frac{1}{\sqrt{a}}\psi\left(\frac{x-b}{a}\right), \quad a, b \in \mathbb{R}, a \neq 0$$

And it is normalized to unity,  $\|\psi^{a,b}\| = \|\psi\| = 1$ .

But first, for a function to be a wavelet, it must pass the admissibility criterion, ie, the constant  $C_\psi$  used in inverse continuous wavelet transform (CWT) must satisfy

$$C_\psi = \int_{-\infty}^{\infty} \frac{|\hat{\psi}(\omega)|^2}{|\omega|} d\omega < \infty$$

In words, a wavelet must have a zero mean and be localized in time and space. Now, the definition of CWT is as follows.

$$(T^{wave} f)(a, b) = \langle f, \psi^{a,b} \rangle = \int dx f(x) |a|^{-1/2} \psi^* \left( \frac{x-b}{a} \right)$$

where  $*$  denotes the complex conjugate. An interpretation is that a function  $f$  can be written as a linear combination of wavelets  $\psi^{a,b}$  with coefficients given by the wavelet transform. The inverse CWT is then defined as

$$f = C_\psi^{-1} \int_{-\infty}^{\infty} \int_{-\infty}^{\infty} \frac{dadb}{a^2} (T^{wave} f)(a, b) \psi^{a,b}$$

### 0.8.2 Haar wavelet

The most basic wavelet is the Haar wavelet. First, we define the dyadic interval on which they are supported.

For each pair of integers  $j, k \in \mathbb{Z}$ , we define the interval

$$I_{j,k} = [2^{-j}k, 2^{-j}(k+1)) = \left[ \frac{k}{2^j}, \frac{k}{2^j} + \frac{1}{2^j} \right)$$

The collection of all such intervals is called the collection of all dyadic subintervals of  $\mathbb{R}$ . It is helpful to note that dyadic interval at scale  $j$  always has length  $|I| = 2^{-j}$ , and so a larger scale  $j$  means a smaller interval width. Also note that  $I_{j,k} = I_{j+1,2k} \cup I_{j+1,2k+1}$ . This is saying that a dyadic interval at scale  $j$  is the union of two dyadic intervals at scale  $j+1$ , and that two adjacent subintervals with scale  $j+1$  split the larger interval into left and right halves.

Dyadic intervals have special properties that come into play when defining the Haar orthonormal system. Given  $j_0, k_0, j_1, k_1 \in \mathbb{Z}$ , with either  $j_0 \neq j_1$  or  $k_0 \neq k_1$ , then either

1.  $I_{j_1, k_1} \cap I_{j_0, k_0} = \emptyset$
2.  $I_{j_1, k_1} \subseteq I_{j_0, k_0}$ , or
3.  $I_{j_0, k_0} \cap I_{j_1, k_1}$

Property 1 leads to orthonormality of Haar wavelet bases as they are supported on dyadic intervals. Properties 2 and 3 state that the smaller dyadic subinterval must either be contained in the left half or right half of a larger dyadic interval.

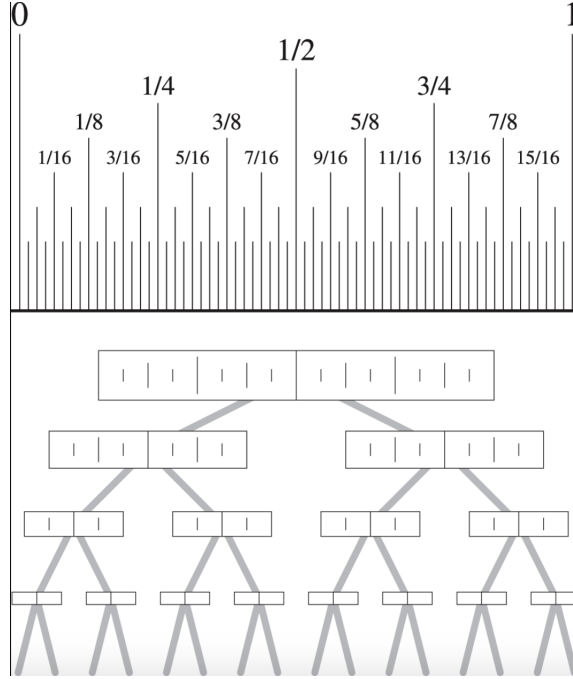


**Figure 19:** A dyadic interval on  $[0, 1]$ . It can also be thought of as a binary tree. Taken from [7].

Now we can define the Haar scaling function (on the interval  $[0, 1]$ ), or the "father" wavelet. Let  $p(x) = \chi_{[0,1]}(x)$ , where  $\chi$  is an indicator function (value 1 on interval, 0 elsewhere), and for each  $j, k \in \mathbb{Z}$ , define

$$p_{j,k}(x) = 2^{j/2} p(2^j x - k) = D_{2^j} T_k p(x)$$

where  $D$  is the dilation operator, and  $T$  is the translation operator. Then the collection  $\{p_{j,k}(x)\}_{j,k \in \mathbb{Z}}$  is the system of Haar scaling functions, and we say for each  $j \in \mathbb{Z}$ , the collection  $\{p_{j,k}(x)\}_{k \in \mathbb{Z}}$  is the system of scale  $j$  Haar scaling functions. In words, the system of Haar scaling functions is the system of dilated and translated  $\chi_{[0,1]}$  that exists on dyadic intervals, and have a constant area of 1.

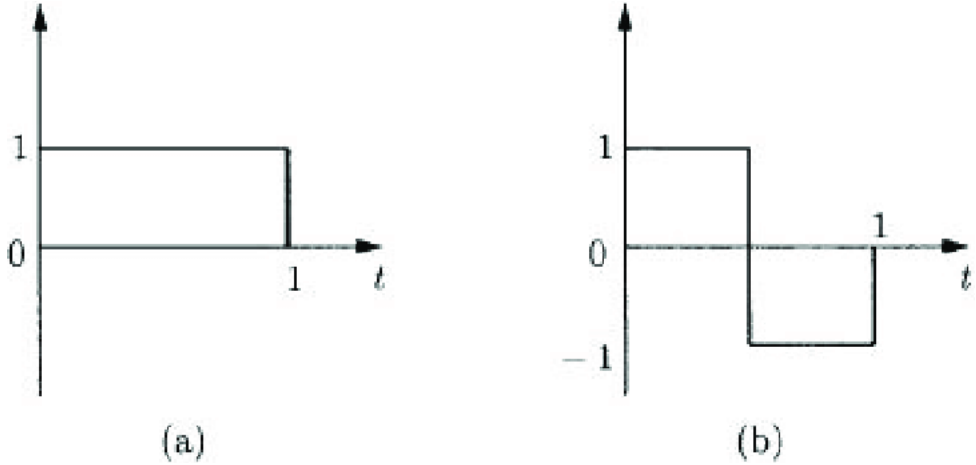


**Figure 20:** (a) Haar scaling function,  $p_{0,0}$  (b) Haar wavelet function,  $h_{0,0}$ . Taken from [7].

Now we can define the Haar wavelet, or the "mother" wavelet.

Let  $h(x) = \chi_{[0,1/2)}(x) - \chi_{[1/2,1)}(x)$ , and for each  $j, k \in \mathbb{Z}$ , define

$$h_{j,k}(x) = 2^{j/2} h(2^j x - k) = D_{2^j} T_k h(x)$$

The collection  $\{h_{j,k}(x)\}_{j,k \in \mathbb{Z}}$  is the Haar system on  $[0, 1]$ , and for each  $j \in \mathbb{Z}$ , the collection  $\{h_{j,k}(x)\}_{k \in \mathbb{Z}}$  is the system of scale  $j$  Haar functions. We see that the Haar wavelet  $h_{j,k}(x)$  is supported on the dyadic interval  $I_{j,k}$ , and so refer to the Haar wavelet function  $h_{j,k}(x)$  as being associated with the interval  $I_{j,k}$ . We have defined both the Haar scaling function and Haar wavelet function on  $[0, 1]$ . Now we can define the Haar system on  $\mathbb{R}$ . Let a fixed scale  $J \in \mathbb{Z}$  be given. The collection

$$\{p_{J,k}(x), h_{j,k}(x) : j \geq J, k \in \mathbb{Z}\}$$

is called the scale  $J$  Haar system on  $\mathbb{R}$ . It can be shown that the scale  $J$  Haar system is a complete orthonormal system on  $\mathbb{R}$ . This allows us to represent any signal as a superposition of the Haar functions and a single Haar scaling function.

### 0.8.3 Other Wavelet Examples

The Morlet wavelet function is defined as

$$\psi_0(\eta) = \pi^{-1/4} e^{i\omega_0 \eta} e^{-\eta^2/2}$$

where  $\eta$  is a non-dimensional "time" parameter, and  $\omega_0$  is the wave number. Observe from the equation that a Morlet wavelet is essentially a sinusoid modulated by a Gaussian to become a "packet" of waves localized in time. The following plots of wavelets produced with Python 'PyWavelets' [8].

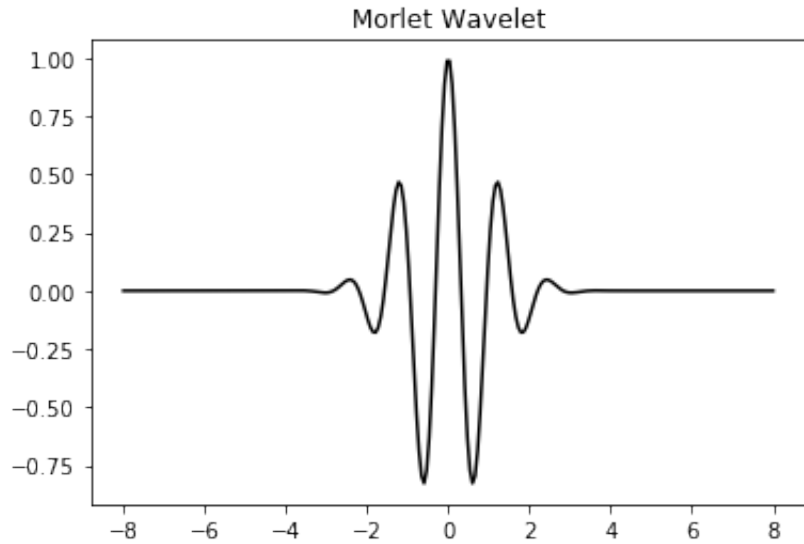


**Figure 21:** An example Morlet wavelet.

The first order derivative of Gaussian wavelet is defined as

$$\psi(t) = -te^{-t^2/2}$$

Because a Gaussian is infinitely differentiable, one can use any derivative of Gaussians (DOG) when performing wavelet transforms. The second-order DOG is also known as the Mexican-hat wavelet.

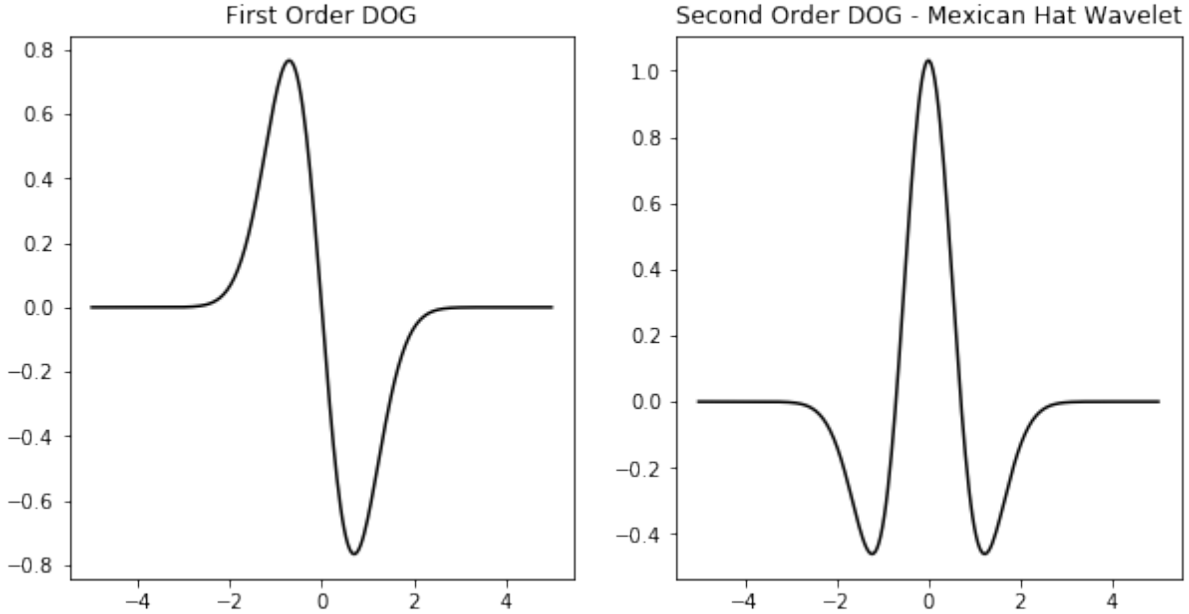


**Figure 22:** First and second order DOG wavelets.

Some other examples include Paul and Debauchies wavelets. There is no clear rule on which mother wavelet to choose when analyzing a signal. As a general rule, one would choose a wavelet that best approximates the features in a desired signal. Also, many wavelet transform software use Morlet wavelets as a default. This is because a Morlet wavelet is conservative middle in terms of localization in time and frequency. For example, Paul < Morlet < Gaussian in terms of frequency resolution, while Gaussian < Morlet < Paul in terms of time resolution [5]. If one were to use a wavelet packet decomposition of a signal (not explained in this report, but the basic idea is to decompose not just the approximation coefficients as in a DWT, but the detail coefficients as well, completing the full decomposition binary tree. The binary tree figure for a DWT is shown in Figure 24), then there exists a Best-Basis algorithm that is designed to find the most optimal wavelet packet basis by minimizing a cost function.

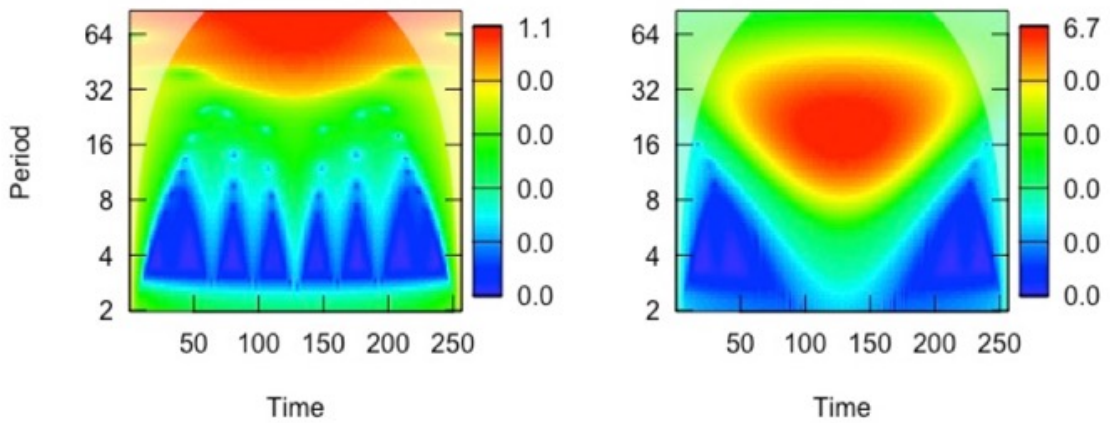


**Figure 23:** Wavelet power spectrum of a (a) Morlet wavelet (b) first order DOG wavelet. [R 'WaveletComp'].

#### 0.8.4 Discrete Haar Transform

First, a motivational example. Suppose one has a signal of length 8, say  $x(t) = \{1, 5, 7, 5, 7, 3, 1, 7\}$ . Now if one had to share this signal with another person, but could only do so with a signal of length 4, what would be the best way? A logical solution would be to average each pair of values, and send the signal  $a(t) = \{3, 6, 5, 4\}$ . Now if we had to reconstruct the original signal  $x(t)$  from  $a(t)$ , what information would we need? Because each value in  $a(t)$  is a pairwise average, it must be equidistant from the original pair of values. Hence, if we had a signal to store the pairwise differences,  $d(t) = \{-2, 1, 2, -3\}$ , then one could fully restore the signal. Specifically, we can recover the original signal by  $x(t) = \{3 + (-2), 3 - (-2), 6 + (1), 6 - (1), 5 + (2), 5 - (2), 4 + (-3), 4 - (-3)\} = \{1, 5, 7, 5, 7, 3, 1, 7\}$ . This is the basic idea behind the Discrete Haar Transform, and more loosely, any DWT.

In a Discrete Haar Transform (DHT), the pairwise averaging is achieved by the Haar scaling function  $\varphi(x)$ , which is analogous to a low-pass filter. The pairwise difference operation is performed by the Haar wavelet function,  $\psi(x)$ , which is analogous to a high-pass filter. The goal is to represent a function  $f(x)$ , say defined on the interval  $[0, 1]$ , in

terms of the Haar system. Given an integer  $J \geq 0$ , we want to achieve

$$f(x) = \sum_{j=J}^{\infty} \sum_{k=0}^{2^j-1} \langle f, h_{j,k} \rangle h_{j,k}(x) + \sum_{k=0}^{2^J-1} \langle f, p_{J,k} \rangle p_{J,k}(x)$$

The second term is an approximation of  $f(x)$  using a scaling function with scale  $J$ , where this scale corresponds to a low resolution approximation. Then, adding all the details/differences (first term) at all scales and positions, we can reconstruct  $f(x)$ .

Define the approximation coefficient at scale  $j$  and position  $k$ ,  $c_j(k)$ , and the detail coefficient at scale  $j$  and position  $k$ ,  $d_j(k)$ , as follows.

$$c_j(k) = \langle f, p_{N-j,k} \rangle, \quad d_j(k) = \langle f, h_{N-j,k} \rangle$$

Recall that for the Haar scaling function  $\varphi$  and the Haar wavelet  $\psi$ , a larger  $j$  corresponds to a smaller dyadic interval on which it is supported. Now, due to the indexing  $N - j$ , a larger  $j$  for the coefficients  $c_j$  and  $d_j$  corresponds to approximations/details on a larger interval/lower resolution.

Now we formally define the DHT. Given  $J, N \in \mathbb{N}$  with  $J < N$  and a finite sequence  $c_0 = \{c_0(k)\}_{k=0}^{2^N-1}$ , the DHT is defined by

$$\{d_j(k) : 1 \leq j \leq J, 0 \leq k \leq 2^{N-j}-1\} \cup \{c_J(k) : 0 \leq k \leq 2^{N-j}-1\}$$

where

$$c_j(k) = \frac{1}{\sqrt{2}} [c_{j-1}(2k) + c_{j-1}(2k+1)], \quad d_j(k) = \frac{1}{\sqrt{2}} [c_{j-1}(2k) - c_{j-1}(2k+1)]$$

and the Inverse DHT is given by

$$c_{j-1}(2k) = \frac{1}{\sqrt{2}} [c_j(k) + d_j(k)], \quad d_{j-1}(k) = \frac{1}{\sqrt{2}} [c_j(k) - d_j(k)]$$

This recursion relation between coefficients is what makes the DHT possible. Recall the earlier example where we wanted to convey a signal  $x(t)$  to another person by storing information of pairwise averages and pairwise differences. We can clearly see the analogy in the formal definition. In the DHT, we take pairwise  $(2k, 2k+1)$  approximation coefficients at a scale  $j-1$  and produce a single value  $c_j(k)$  which is at a scale  $j > j-1$ ,

hence at a lower resolution (taking a size 8 signal and averaging it to a signal of size 4). Likewise, for the detail coefficient  $d_j(k)$ , we take pairwise approximations of a function at a smaller scale and take the difference.

The DHT can be expressed as a matrix operation, which makes it more intuitive to understand. Given  $L \in \mathbb{N}$  even, define  $(\frac{L}{2}) \times L$  matrices  $\mathbf{H}_L, \mathbf{G}_L$  by

$$\mathbf{H}_L = \frac{1}{\sqrt{2}} \begin{pmatrix} 1 & 1 & 0 & 0 & 0 & \dots & 0 \\ 0 & 0 & 1 & 1 & 0 & \dots & 0 \\ & & & & & \vdots & \\ 0 & 0 & 0 & \dots & 0 & 1 & 1 \end{pmatrix} \quad \mathbf{G}_L = \frac{1}{\sqrt{2}} \begin{pmatrix} 1 & -1 & 0 & 0 & 0 & \dots & 0 \\ 0 & 0 & 1 & -1 & 0 & \dots & 0 \\ & & & & & \vdots & \\ 0 & 0 & 0 & \dots & 0 & 1 & -1 \end{pmatrix}$$

$\mathbf{H}_L$  is the approximation matrix, computing pairwise averages.  $\mathbf{G}_L$  is the detail matrix, computing pairwise differences. We define the  $L \times L$  matrix  $\mathbf{W}_L$ , the wavelet matrix, by

$$\mathbf{W}_L = \begin{pmatrix} \mathbf{H}_L \\ \mathbf{G}_L \end{pmatrix}$$

Then, given  $J, N \in \mathbb{N}$  with  $J < N$  and length  $2^N$  vector  $\mathbf{c}_0 = (c_0(0), c_0(1), \dots, c_0(2^N - 1))$ , the DHT of  $\mathbf{c}_0$  is the vector  $(\mathbf{d}_1, \mathbf{d}_2, \mathbf{d}_3, \dots, \mathbf{d}_J, \mathbf{c}_J)$ , where

$$\begin{pmatrix} \mathbf{c}_j \\ \mathbf{d}_j \end{pmatrix} = \begin{pmatrix} \mathbf{H} \\ \mathbf{G} \end{pmatrix} \mathbf{c}_{j-1}$$

with  $\mathbf{H}, \mathbf{G}$  are  $2^{N-j} \times 2^{N-j+1}$ , with  $1 \leq j \leq J$ . The Inverse DHT is given by

$$\mathbf{c}_{j+1} = \mathbf{H}^* \mathbf{c}_j + \mathbf{G}^* \mathbf{d}_j$$

The DHT (and DWT in general) can be visualized as a tree diagram shown in Figure 24. First, given a signal  $\mathbf{c}_0$  of length  $N$ , we apply the approximation and detail matrices  $\mathbf{H}, \mathbf{G}$  combined as a single matrix  $\mathbf{W}$ . The  $\mathbf{H}$  gives us approximation coefficients  $\mathbf{c}_1$  of length  $\frac{N}{2}$ , and  $\mathbf{G}$  gives us the detail coefficients  $\mathbf{d}_1$  of length  $\frac{N}{2}$ . We keep the detail coefficient  $\mathbf{d}_1$ , and apply  $\mathbf{W}$  to  $\mathbf{c}_1$  only. This gives us coefficients  $\mathbf{c}_2, \mathbf{d}_2$ , both length  $\frac{N}{2^2}$ . We keep  $\mathbf{d}_2$  and repeat. We continue this wavelet "decomposition" to a desired level or until the length of the approximation coefficient can no longer be halved.

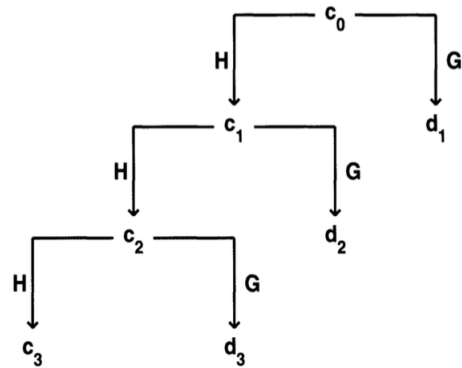


**Figure 24:** A tree diagram illustrating the DHT. Taken from [22].

Hence, you end up with a single approximating function at a fixed low resolution

$$c_J = \sum_{k=0}^{2^J-1} \langle f, p_{J,k} \rangle p_{J,k}(x)$$

plus details at varying scales

$$\sum_{j=J}^{\infty} \sum_{k=0}^{2^j-1} \langle f, h_{j,k} \rangle h_{j,k}(x)$$

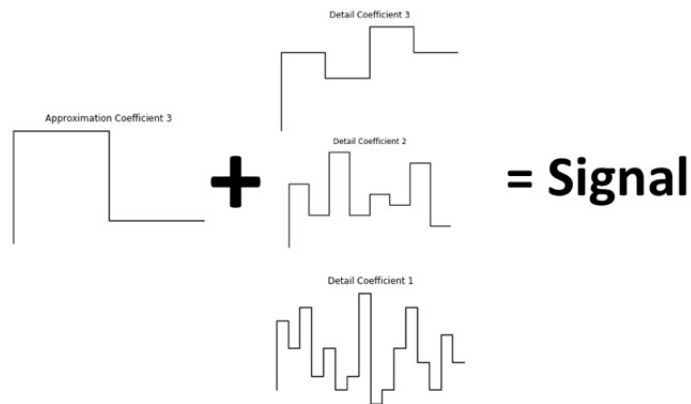


**Figure 25:** A visual interpretation of a DHT and its coefficients .

The approximation coefficients of the DHT of a signal of length  $2^4$  are shown below. DWT was applied with Python package 'PyWavelets' [8].

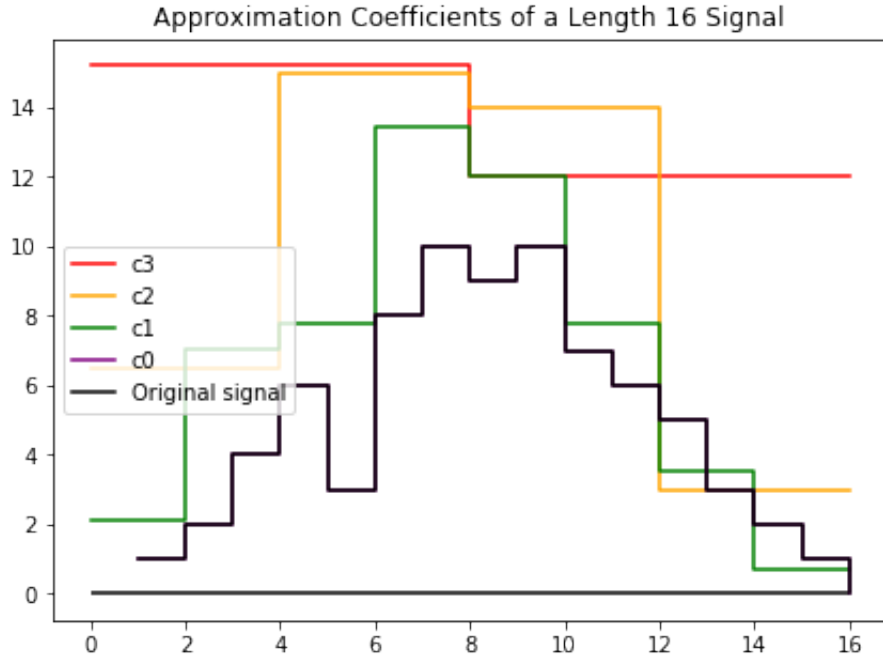


**Figure 26:** Approximation coefficients at each level of decomposition.  $c_0$  is the original signal. DHT would progress from  $c_0$  to  $c_3$ , as the high resolution details are stored in detail coefficients and the progressively lower resolution information is stored in the approximation coefficients. Inverse DHT, given all detail coefficients and  $c_3$ , reconstructs the original signal.

### 0.8.5 Discrete Wavelet Transform

(This section might have errors, I had to go through the Introduction to Wavelet Analysis quickly so I still do not perfectly understand MRA and the DWT. This is my best interpretation.) Before going into DWT, one should study multi-resolution analysis (MRA), Chapter 7 of Introduction to Wavelet Analysis [24]. MRA allows one to construct their own wavelets (satisfying some conditions), and apply DWT.

The discrete wavelet transform (DWT) essentially uses the idea outlined in the DHT. The DWT of a length  $M = 2^N$  signal can be thought of as a linear transformation of the M-vector

$$\mathbf{c}_0 = [c_0(0), c_0(1), \dots, c_0(M-1)]$$

into the M-vector

$$\mathbf{d} = [\mathbf{d}_1, \mathbf{d}_2, \dots, \mathbf{d}_J, \mathbf{c}_J]$$

with

$$\mathbf{d}_j = [d_j(0), d_j(1), \dots, d_j(2^{-j}M - 1)], \quad \mathbf{c}_J = [c_J(0), c_J(1), \dots, c_J(2^{-J}M - 1)]$$

In DWT, the  $l^2$  sequence of coefficients  $\{h(k)\}$  which satisfy

$$\varphi(x) = \sum_k h(k) 2^{1/2} \varphi(2x - k)$$

on  $\mathbb{R}$ , where  $\varphi$  is the scaling function associated with a given MRA  $\{V_j\}$ , is called the scaling filter associated with  $\varphi$ . Then, define the wavelet filter

$$g(n) = (-1)^n \overline{h(1-n)}$$

Once we have the scaling filter  $h(k)$  and the wavelet filter  $g(n)$ , we can define the scaling function and the wavelet function as follows.

$$\varphi(x) = \sum_n h(n) \varphi_{1,n}(x)$$

and the corresponding wavelet function

$$\psi(x) = \sum_n g(n) \varphi_{1,n}(x)$$

Now, we can formally define the DWT.

Define the scaling filter  $h(k)$ , scaling function  $\varphi$ , wavelet filter  $g(n)$  and the wavelet function  $\psi(x)$  as above. Given  $f(x)$ ,  $L^2$  on  $\mathbb{R}$ , define for  $k \in \mathbb{Z}$ ,

$$c_0(k) = \langle f, \varphi_{0,k} \rangle$$

and for every  $j \in \mathbb{N}, k \in \mathbb{Z}$ ,

$$c_j(k) = \langle f, \varphi_{-j,k} \rangle, \quad d_j(k) = \langle f, \psi_{-j,k} \rangle$$

Then, the recursion relations between coefficients used in DWT are

$$c_{j+1}(k) = \sum_n c_j(n) \overline{h(n-2k)}, \quad d_{j+1}(k) = \sum_n c_j(n) \overline{g(n-2k)}$$

and

$$c_j(k) = \sum_n c_{j+1}(n)h(k-2n) + \sum_n d_{j+1}(n)g(k-2n)$$

Again, it is more intuitive to see the approximation and detail matrices. Let  $h(k)$  be a real valued scaling filter of length 4, define the wavelet filter  $g(k) = (-1)^k h(3-k)$ , and a signal of length 8. Then

$$\mathbf{H}_8 = \begin{pmatrix} h(0) & h(1) & h(2) & h(3) & 0 & 0 & 0 & 0 \\ 0 & 0 & h(0) & h(1) & h(2) & h(3) & 0 & 0 \\ 0 & 0 & 0 & 0 & h(0) & h(1) & h(2) & h(3) \\ h(2) & h(3) & 0 & 0 & 0 & 0 & h(1) & h(2) \end{pmatrix}$$

and

$$\mathbf{G}_8 = \begin{pmatrix} g(0) & g(1) & g(2) & g(3) & 0 & 0 & 0 & 0 \\ 0 & 0 & g(0) & g(1) & g(2) & g(3) & 0 & 0 \\ 0 & 0 & 0 & 0 & g(0) & g(1) & g(2) & g(3) \\ g(2) & g(3) & 0 & 0 & 0 & 0 & g(1) & g(2) \end{pmatrix},$$

Then, constructing the wavelet matrix  $\mathbf{W}$  as in DHT, a first level decomposition of M-vector  $\mathbf{c}_0$  yields coefficients at level 1,

$$\mathbf{W}_M \mathbf{c}_0 = \begin{pmatrix} \mathbf{d}_1 \\ \mathbf{c}_1 \end{pmatrix}$$

In the second step/level,

$$\begin{pmatrix} \mathbf{I}_{(M/2)} & 0 \\ 0 & \mathbf{W}_{M/2} \end{pmatrix} \begin{pmatrix} \mathbf{d}_1 \\ \mathbf{c}_1 \end{pmatrix} = \begin{pmatrix} \mathbf{d}_1 \\ \mathbf{d}_2 \\ \mathbf{c}_2 \end{pmatrix}$$

where  $\mathbf{I}$  is a  $M/2 \times M/2$  identity matrix, there to preserve information on the detail matrix, and apply the wavelet matrix only to the approximation coefficients. In general, the  $j^{th}$  step is

$$\begin{pmatrix} \mathbf{I}_{1-2^{-j}} & 0 \\ 0 & \mathbf{W}_{2^{-j}M} \end{pmatrix} \begin{pmatrix} \mathbf{d}_1 \\ \vdots \\ \mathbf{d}_{j-1} \\ \mathbf{c}_j \end{pmatrix} = \begin{pmatrix} \mathbf{d}_1 \\ \vdots \\ \mathbf{d}_{j-1} \\ \mathbf{d}_j \\ \mathbf{c}_j \end{pmatrix}$$

So far we have only worked with signals that are of length  $2^N$  for some  $N \in \mathbb{N}$ . What happens if our signal is not a power of 2? There are several ways to deal with this. The two main methods are zero padding and periodization.

In zero padding, we simply make the signal to have a length of power of 2 by appending 0's on both ends, as such:  $\{0, 0, 0, 0, 5, 2, 7, 4, 7, 43, 4, 7, 2, 0, 0, 0\}$ . This introduces artificially diminished wavelet powers at the ends of signal, leading to the requirement of the cone of influence, described in the next section. Periodization is, as it suggests, extending the signal such that it is a periodic signal of length that is a power of 2.

### 0.8.6 Wavelet Power Spectrum

The wavelet power spectrum is a powerful visual tool, but more than that, it is used in the significance testing described in the next section. The wavelet power spectrum displays the wavelet power of a signal, with frequency/period/scale of the *daughter wavelet* in the vertical axis, and time in the horizontal axis. Recall the definition of CWT. Defining  $a$  as the scale parameter and  $b$  as the translation parameter, the CWT of a time series  $x(t)$  is

$$W(b, a) = \frac{1}{\sqrt{a}} \int_{-\infty}^{\infty} x(t) \psi^* \left( \frac{t-b}{a} \right) dt$$

The wavelet power is then the quantity  $|W(b, a)|^2$ . In implementation, the integral is a summation over  $N$  samples in the time series, and the computation is actually done in the Fourier domain. A step-by-step guide is in Schulte.

The cone of influence (COI) is a special area of the spectrum, especially prominent in the lower frequency regions (larger scale parameter  $a$ ). This is a region where the wavelet extends beyond the observed region of the signal when applying wavelet transform and edge effects cannot be ignored. One must be cautious when interpreting spectrum features in the COI. For example, if one zero-pads a finite signal when performing DWT, then when the daughter wavelet is being multiplied with the signal near the ends, the zeros diminish the power within the COI.

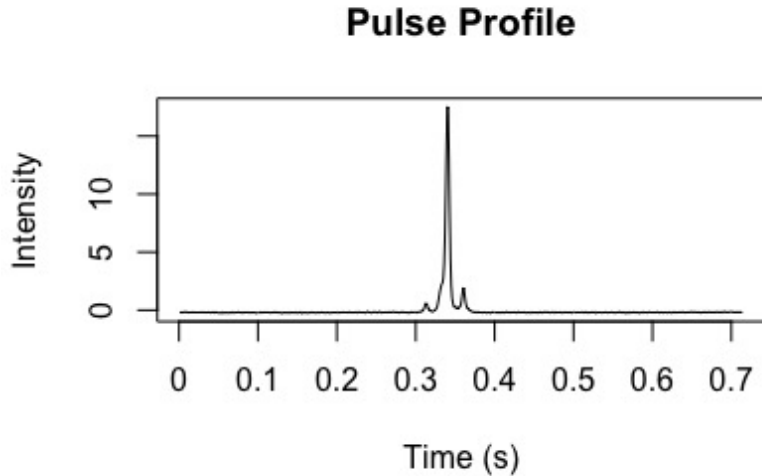


**Figure 27:** J0332+5434 pulse profile with period of 0.714 seconds. [R]

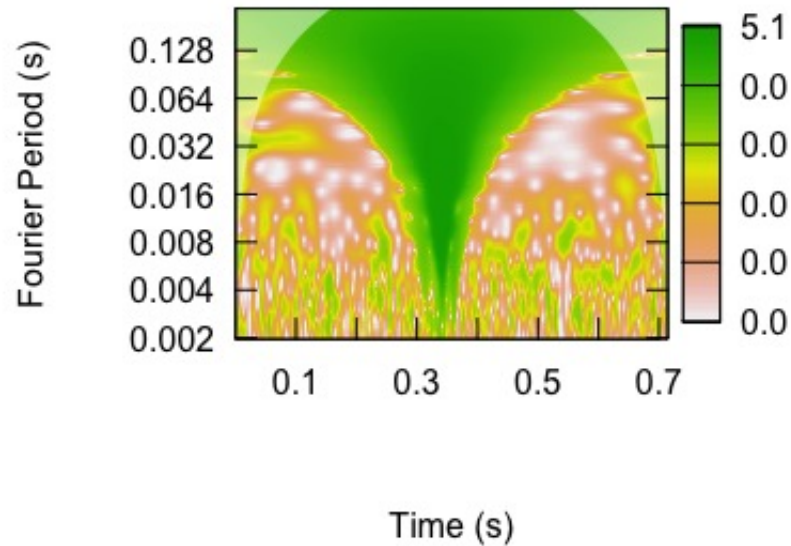


**Figure 28:** Wavelet power spectrum of above profile. COI is the light gray shading at the corners. [R 'WaveletComp']

Interpreting the horizontal axis, time, is pretty straightforward. The vertical axis, in this figure shown as period, is sometimes confusing. First, remember that this is a plot of the timescale plane, with scale converted to period. Hence, the period on the vertical axis denotes the length of the daughter wavelet in time units. Now recall Figure 18 and that a wavelet transform obtains good frequency localization at lower frequencies at the

expense of time localization, while obtaining good time localization at higher frequencies at the expense of frequency localization. This is clearly visible in the spectrum above. First, note that if the vertical axis were converted into frequency ( $1/\text{period}$ ), as we go up, frequency would decrease. Now observe that at higher frequencies (lower on the vertical axis), the contour patches are stretched along the frequency direction. Thus it has very precise time localization, but not so much in the frequency domain. Meanwhile, at lower frequencies (higher on the vertical axis), patches begin to stretch along the time direction. Hence at lower frequencies, wavelet transform has precise frequency localization but not so much in the time domain.

Unrelated to this project but an interesting application of wavelet transforms is signal denoising. Referring back to the DWT tree diagram (Figure 24), if one sets the last level detail coefficient values to zero, then take the inverse DWT, the reconstructed signal is now missing features at small wavelet scales. By making a desired number of detail coefficients to zero and reconstructing the signal, it is possible to remove noise. However, this is assuming that ignored detail coefficients only contain noise information, and zero signal features of interest. Figure 29 depicts denoising of ECG data. 'PyWavelets' was used to obtain ECG data and perform DWT.

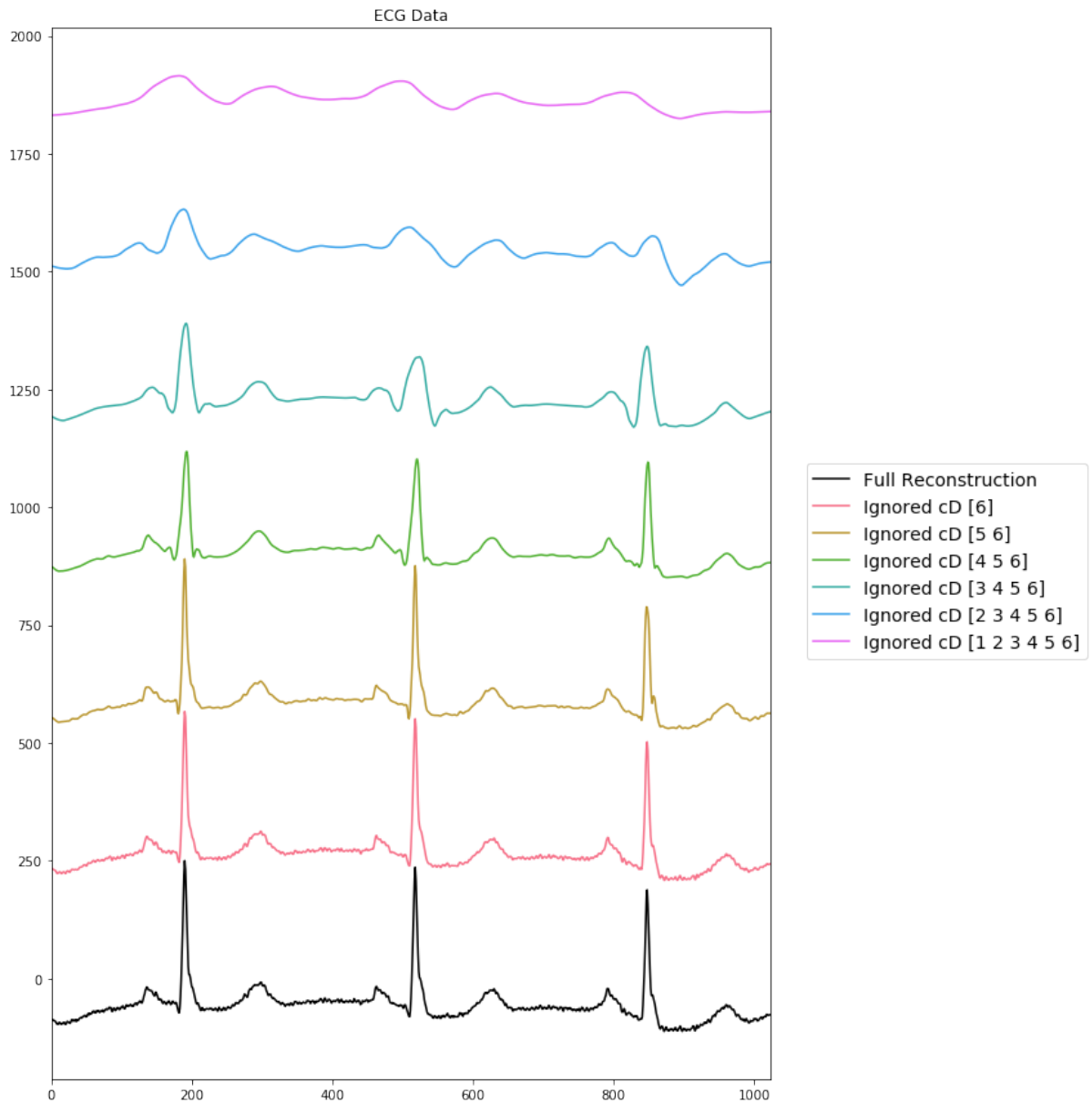


**Figure 29:** Denoising of ECG data. Bottom signal is the original data. Progressing up, we ignore more and more of detail coefficients cD, produced from DWT using a Symlets wavelet.

## 0.9 WAVELET SIGNIFICANCE TESTING

### 0.9.1 Pointwise Testing

The first step-by-step significance testing in wavelet analysis was introduced by Torrence and Compo [23]. The method is commonly referred to as pointwise significance test-

ing. The basic idea is this: define the set containing all points in a wavelet spectrum as  $H$ . One then picks a background noise representing the null hypothesis, performs thousands of Monte Carlo simulations of the noise, takes wavelet transforms, and plots the distribution of wavelet powers (or whatever the desired wavelet quantity is, eg., wavelet coherency). The critical power corresponding to a pointwise significance level  $\alpha_{pw}$  is simply the  $1 - \alpha_{pw}$  th percentile of the Monte Carlo distributions. Then, one compares each point in  $H$  against this critical value, hence the name "pointwise".

Here is a more detailed outline, well summarized in [18]. I will only consider the wavelet power from here on. For each point in  $H$ , assign a p-value,  $\rho_{pw}$ , the probability of observing an equal or more extreme wavelet power if the null hypothesis (say pure WN) is true. The test then returns a subset of  $H$ ,

$$P_{pw} = \{(b, a) : \rho_{b,a}(b, a) < \alpha_{pw}\}$$

which is the set of all points that are pointwise significant. Typically, in a power spectrum, groups of pointwise significant points are encircled by a contour which is a function of  $\alpha_{pw}$ . The encircled area is referred to as patches.

The issue with pointwise testing is that it produces many spurious patches, as depicted in Figure 30 [14]. The following sections describe areawise, geometric, and cumulative areawise tests, designed to reduce the number of false positives.

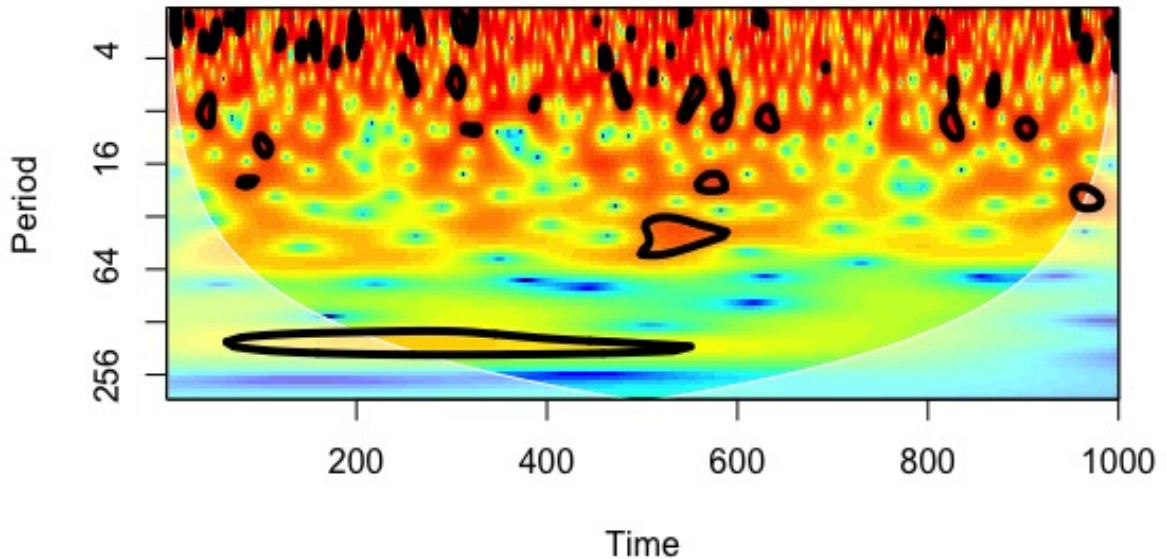


**Figure 30:** Power spectrum of pure WN signal against a null hypothesis of pure WN. Pointwise testing falsely identifies many patches as significant at  $\alpha_{pw} = .05$ . [R ‘biwavelet’]

### 0.9.2 Areawise Testing

Maraun et al. [14] developed the areawise test to reduce spurious patches. It was noted in an earlier paper Maraun and Kurth (2004) that points in  $H$  in the timescale plane are correlated. Given two points,  $(b, a), (b', a') \in H$ , the correlation between the two points' coefficients is represented by the reproducing kernel

$$K(b, a, b', a') = \frac{1}{C_\psi \sqrt{(aa')}} \int \left[ \psi\left(\frac{t-b}{a}\right) \psi^*\left(\frac{t-b'}{a'}\right) \right] dt$$

where  $C_\psi$  is the admissibility constant, and  $\psi$  is the mother wavelet. Then, the wavelet coefficient at  $(b, a)$  is

$$W(b, a) = \int \int K(b, a, b', a') W(b', a') \frac{da' db'}{a'^2}$$

where  $K(b, a, b', a')$  can be thought of as a weight multiplying the neighboring point's wavelet coefficient  $W(b', a')$ . Hence, information from neighboring points is captured. This leads to the idea that spurious patches arise in clusters due to the correlations in coefficients. We can use the fact that typical spurious patches have an area similar to that of the kernel at the position  $(b, a)$  to reduce false positives.

First, we define areawise significant patches [14,18]. Given all pointwise significant patches  $P_{pw}$ , choose a critical area  $P_{crit} \subset H$  for which the reproducing kernel, when dilated and translated to  $(b, a)$ , exceeds some critical level  $K_{crit}$ ,

$$P_{crit}(b, a) = \{(b', a') : K(b, a, b', a') > K_{crit}\}$$

Then the set of all points whose wavelet power is areawise significant (on top of being pointwise significant) is

$$P_{aw} = \bigcup_{P_{crit}(b, a) \subset P_{pw}} P_{crit}(b, a)$$

Essentially, given a pointwise significant patch, a point  $(b, a)$  inside this patch is also areawise significant if the reproducing kernel, dilated and translated to  $(b, a)$ , fits completely in the patch. An issue with areawise testing, however, is that determining the critical area corresponding to  $\alpha_{aw}$  requires a root finding algorithm which is computationally expensive.

### 0.9.3 Geometric Testing

In order to avoid this root finding algorithm, Schulte et al. [16] developed the geometric test. The key was to define a new test statistic,  $A_{norm}$ , which is the normalized area of a pointwise significant patch,  $A_{patch}$ .

$$A_{norm} = \frac{A_{patch}}{\hat{a}^2}$$

where  $\hat{a}^2$  is the patch's mean scale coordinate, detailed in his paper. The division accounts for a patch's expansion in time and scale direction as scale increases (toward lower frequency). Hence, one can compare areas of any patch anywhere in  $H$  through this normalization. Areawise significance testing steps are as follows.

First, generate many wavelet spectra under some null hypothesis, say WN through Monte

Carlo simulation. Next, compute the null distribution of  $A_{norm}$  using patches in the spectra. Then, one can find the critical  $A_{norm}$  corresponding to some geometric significance level  $\alpha_{geo}$  by computing  $1 - \alpha_{geo}$  th percentile of the null distribution.

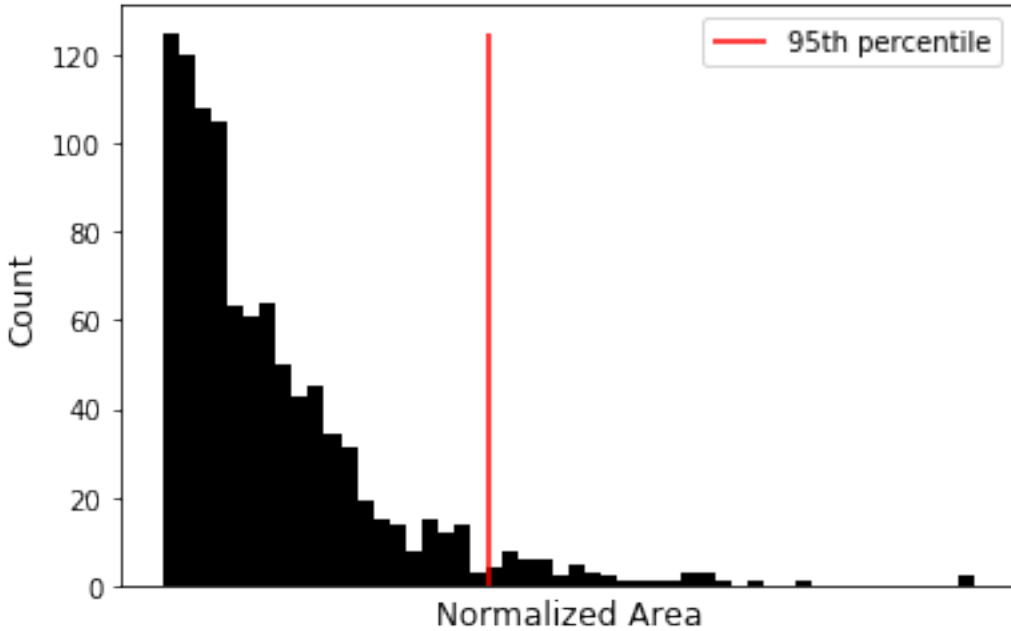


**Figure 31:** Value of normalized area at the 95th percentile of Monte Carlo simulations is the critical  $A_{norm}$  corresponding to  $\alpha_{geo} = .05$ . In practice, one would fit a distribution to the histogram and then take the 95th percentile.

#### 0.9.4 Cumulative Areawise Testing

The issue with both the areawise and geometric testing is that one needs to select two different significant levels,  $\alpha_{pw}$  and  $\alpha_{aw}$  or  $\alpha_{geo}$ . Thus, interpretation of the significance of a patch is not clear. For example, is a patch that is significant at  $(\alpha_{pw} = .05, \alpha_{geo} = .01)$  more significant than one at  $(\alpha_{pw} = .01, \alpha_{geo} = .05)$ ? Hence, an improvement to the geometric test was introduced in Schulte (2016) [17]. The idea was to study how the geometric and topological characteristics of a patch change as  $\alpha_{pw}$  varied. I will try to explain the test here, but there are a lot of details which describe the topological ideas in [17] that won't be discussed in this report. Figure 4 depicting topological evolution and Figure 9 depicting geometric pathways in [17] are especially helpful in understanding the test.

First, given pointwise significant patches, the goal of this test is to assess changes in

the normalized area  $A_{norm}$  defined previously for each point in  $H$ , as **pointwise** significance  $\alpha$  varies over  $\alpha_1, \alpha_2, \dots, \alpha_N$ . If we choose  $N$  pointwise significance levels such that  $\alpha_1 < \alpha_2 < \dots < \alpha_N$ , then the sets

$$P_{pw}^i = \{(b, a) : \rho_{pw}(b, a) < \alpha_i\}$$

form a filtration of  $H$ ,

$$\emptyset = P_{pw}^1 \subseteq P_{pw}^2 \subseteq \dots \subseteq P_{pw}^N = H$$

for sufficiently small  $\alpha_1$  and sufficiently large  $\alpha_N$ . Given a single point  $x \in H$ , the local filtration about  $x$  forms a geometric pathway. Formally, a geometric pathway  $G_x$ , corresponding to a point  $x \in H$ , is a nested sequence

$$\emptyset = P_1^x \subseteq P_2^x \subseteq \dots \subseteq P_N^x = H$$

with

$$P_i^x = \{(b, a) : (b, a) \in P_{pw}^i, (b, a) \sim x\}$$

where  $\sim$  denotes an equivalence relation. The meaning of equivalence relation between two points  $x, (b, a) \in H$  is defined in the paper as well. In words, given a single point  $x \in H$ , begin at the lowest significance level, say  $\alpha_1 = .10$ . Many pointwise significant patches may appear. We sum up the normalized area  $A_{norm}$  of only the patch with which  $x$  belongs in. Now repeat this for increasing set of pointwise significance levels, say  $\alpha_2 = .01, \alpha_3 = .03, \dots, \alpha_N = .15$ , for all points in  $H$ . Then the total sum of  $A_{norm}$ , or cumulative normalized area, for each point is our test statistic. Each point is assigned a total normalized area integrated over  $G_x$ , or a "set of discrete pointwise significance levels". Hence, the name cumulative areawise testing. A visual interpretation of the test is shown in Figure 32.

Now, a step by step procedure for cumulative areawise testing. First, pick a set of discrete pointwise significance levels,  $\alpha_1, \alpha_2, \dots, \alpha_N$ , and a point  $x \in H$ , to perform the test on. Second, calculate normalized areas  $A_1^x, A_2^x, \dots, A_N^x$  corresponding to  $N$  members of  $G_x$ . Assume  $A_i^x = 0$  if  $P_i^x = \emptyset$  (point  $x$  does not belong to any patches) or  $P_i^x = \{x\}$  (the point  $x$  is a patch by itself). Third, compute the sum  $A^x = \sum_{k=1}^N A_k^x$ , and compare this to some critical area  $A_{crit}$  obtained from Monte Carlo method. Finally, repeat this  $\forall x \in H$ . To obtain  $A_{crit}$ , similar to previous tests, generate thousands of wavelet spectra and geometrical pathways under some null hypothesis, calculate the null distribution, and compute

the  $1 - \alpha_c$  th percentile, where  $\alpha_c$  is the desired significance of the cumulative test.

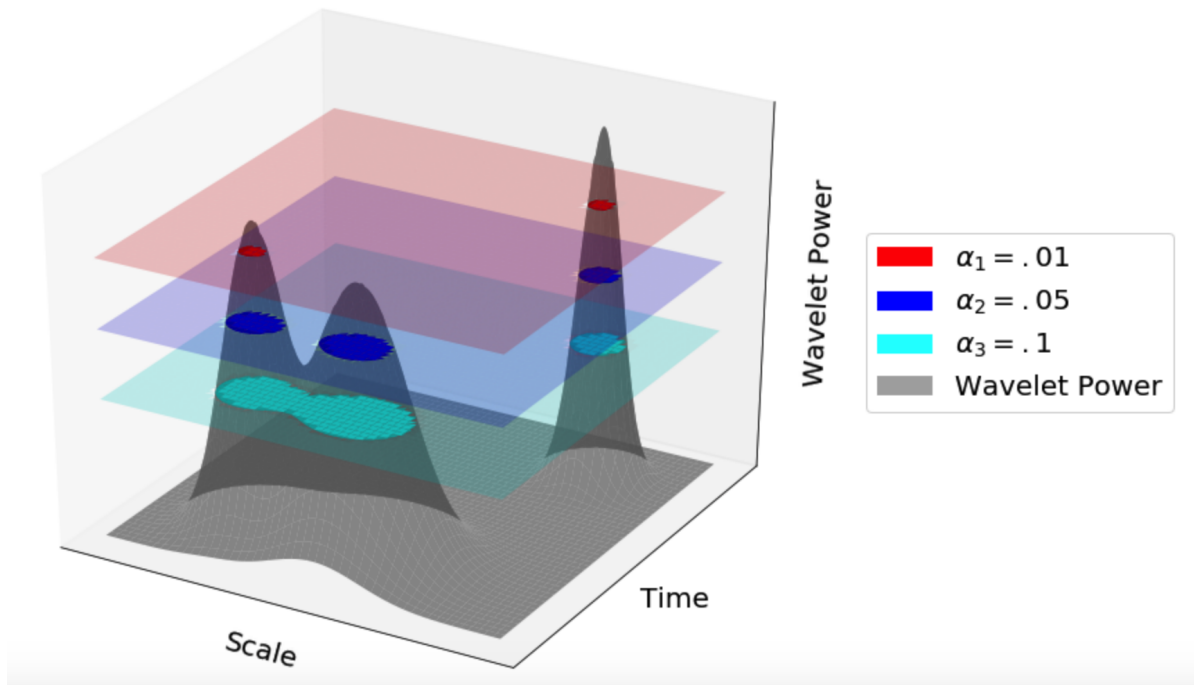


**Figure 32:** Interpretation of cumulative areawise testing as a filtration of  $H$ . Each colored area of intersection corresponds to a pointwise significant patch at the associated  $\alpha_{pw}$  shown in legend.

Let's imagine we applied cumulative areawise testing to the figure above. The grey surface represents the wavelet power of a signal in the timescale plane. A bivariate Gaussian with a tall height corresponds to a significant feature. Suppose we pick a point  $x = (b, a)$  on the timescale plane that is at the center of the leftmost Gaussian, and a set of pointwise significance levels  $\alpha_1 = .01$ ,  $\alpha_2 = .05$ , and  $\alpha_3 = .1$ . Begin by applying pointwise testing with  $\alpha_3 = .1$ . The test returns cyan patches shown in the figure as significant. Because  $x$  belongs in the left cyan patch, we add the normalized area,  $A_x^3$ , to our test statistic  $A^x$ . However, we *do not* add the area of the cyan patch on the right, as the point  $x$  does not belong to the patch. Now, we apply pointwise testing to the spectrum with  $\alpha_2 = .05$ . Our significance level has decreased from  $.1$  to  $.05$ , hence we are applying a more strict condition. This can be visualized as the blue plane, which is higher than the cyan plane and hence requires wavelet power to be larger to be considered significant. As such, the pointwise significant patches, colored in blue, have smaller area. In fact, the leftmost cyan patch has now separated into two separate blue patches. When we now add the normalized area  $A_x^2$  to our test statistic  $A^x$ , we only add that of the leftmost blue patch,

as our point  $x$  only belongs to that patch. Repeat for  $\alpha_1 = .01$ , which introduces even smaller patches.

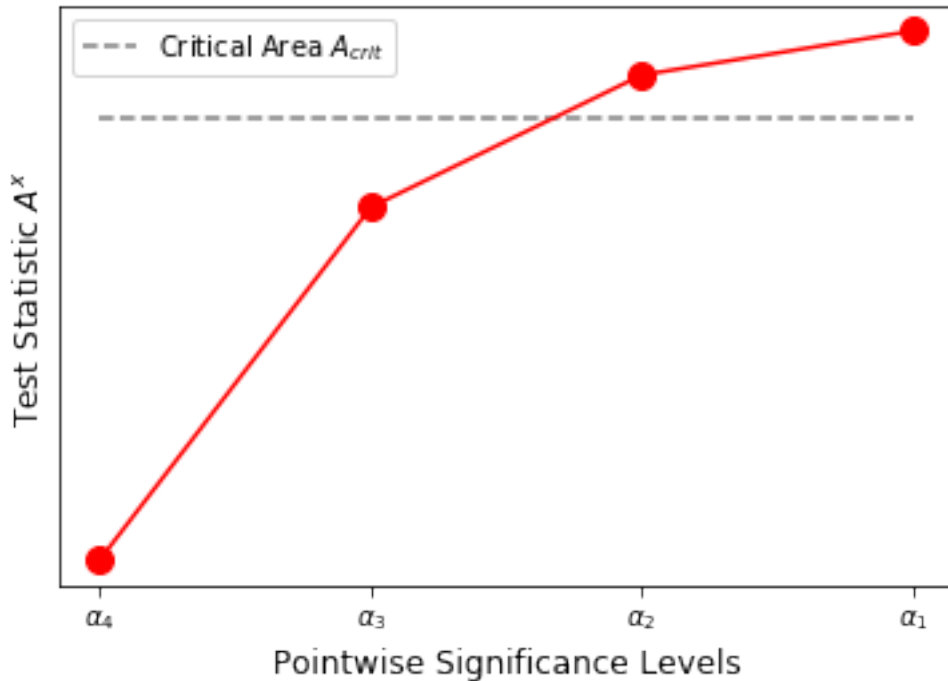


**Figure 33:**  $A^x$  as it iterates over some specified pointwise significance levels.

As we perform the filtration procedure,  $A^x$ , the test statistic of the point, might vary as shown in Figure 33. If the final  $A^x > A_{crit}$ , then that point is considered cumulative areawise significant.

So how does one pick the set of pointwise significance levels? Schulte [17] suggested  $\alpha_1 = 0.02$ ,  $\alpha_N = 0.18$ ,  $\Delta\alpha = 0.02$  to increase computational efficiency. It was also noted that  $\Delta\alpha_1 < .02$  did not increase detection of true positives, but  $\Delta\alpha_1 > 0.03$  decreased true positive detection. Also note that Schulte [18] outlines a simplified version of the cumulative areawise testing which makes it computationally more efficient to implement. I won't discuss it in this report, but it's useful in understanding how the R package 'advbiwavelet' detects contours and patches.

### 0.9.5 Other Significance Tests

Even though I didn't apply them, there are two more useful tests. The first is cumulative arc-wise testing, introduced in Schulte (2019) [18]. This test is designed solely for detect-

ing periodicities in a signal, and outperforms areawise and cumulative areawise testing in this task. The test acts on the assumption that periodicities in a signal produce long, narrow patches stretched along the time axis, depicted in Figure 34. The test uses lengths of these significant patches, hence the name arc-wise.

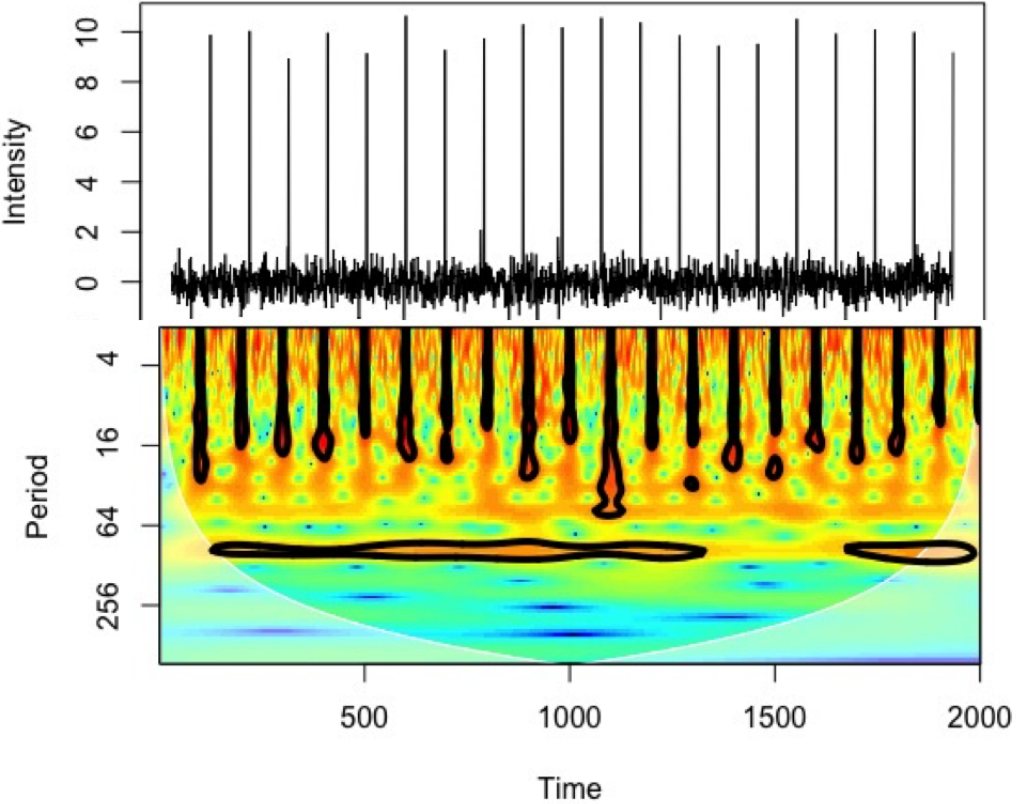


**Figure 34:** A white noise signal with a periodic singularity every 100s. A singularity produces a narrow patch stretched along the scale axis. The periodicity of the signal produces an arc along the time axis, which we know must be located at a period of 100s. Note that the contour shown is not from the application of a cumulative arcwise testing, but only pointwise. [R 'advbiwavelet']

First, one fixes a scale  $a$  and a pointwise significance level  $\alpha_{pw}$ . Apply the pointwise significance testing and identify pointwise significant arcs at this fixed scale. Next, compute the normalized arc length, which is equal to  $\frac{\text{Number of points in the arc}}{\text{fixed scale } a}$ . Dividing by the scale accounts for the fact that at larger scales (lower frequencies), patches tend to stretch in both time and scale direction. Third, we repeat this for all scales. Finally, we repeat the previous three steps for a finite set of pointwise significance levels  $\alpha_1, \alpha_2, \dots, \alpha_N$  and sum the arc lengths. For each  $x \in H$ , we have assigned a cumulative arc length, which is our test statistic. Similar to the other tests, a Monte Carlo method can be used to determine

a critical arc-length.

This test could potentially be used to identify the characteristic period of mode changes, if it exists. However, one would have to connect numerous profile data as a single time series, which might be very discontinuous, as well as very long.

The second test is topological significance testing, first introduced in by Schulte [16] and very well summarized in [18]. This test is ideally used together with cumulative area-wise testing to extract extra information from a signal. While I won't go in detail here, there two main statistics of concern. One of them is Betti number  $\beta_1$ , which is the number of holes on a topological surface. Holes are regions in  $H$  which are fully surrounded by points in  $P_{pw}$ . One can plot the mean number of holes from Monte Carlo simulation and a given signal as a function of varying pointwise significance levels to determine if the signal is distinguishable from the null distribution.

Holes are of particular interest in this report. It is explained in section 0.10.2. First, recall that spurious patches typically arise from the reproducing kernel, which is smooth. This means kernels do not produce holes, especially at low pointwise significance levels. However, when two fluctuations are located nearby in time and frequencies, it may cause holes in a patch. Hence, holes in a patch often indicate a significant feature in the signal

MJD: 58411,  $\alpha_{pw}$ : 0.99,  $\alpha_{cum}$ : 0.99

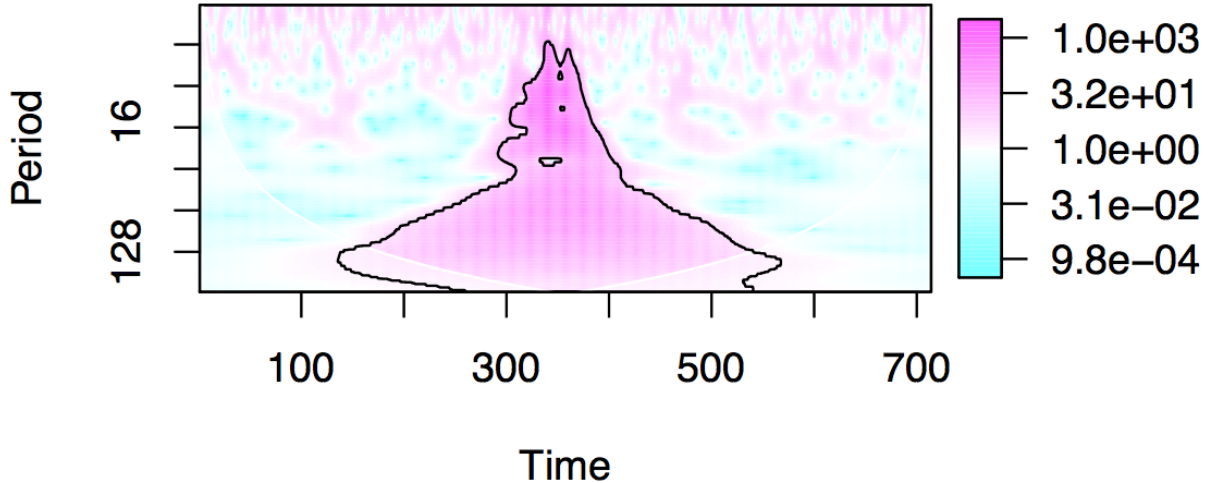


**Figure 35:** Power spectrum of the difference between two J0332+5434 profiles. Holes are visibly present, indicating a significant feature exists in the profile differences. [R 'advbiwavelet']

## 0.10 APPLICATION TO J0332+5434

The papers discussed in the previous sections applied wavelet analysis in the context of climatology, whose typical null distribution is modeled by red noise (RN) [14,16,17,18,23]. Hence, the Monte Carlo simulations of RN was generated by a first-order auto regressive model,  $x_n = \rho x_{n-1} + w_n$  [23]. In general, AR( $p$ ), an autoregressive model of order  $p$ , is defined as

$$x(n) = c + \sum_{i=1}^p \rho_i x_{n-i} + w_n$$

where  $c$  is a constant,  $\rho$  denotes the coefficients/parameters of the model, and  $w_n$  is WN. Pure WN, which is the background noise we want in our context, can be achieved then by simply setting the coefficients to zero.

Wavelet analysis was applied in two different ways, on the ratio of profiles and the difference of profiles. The test was applied using R 'biwavelet' [20] and 'advbiwavelet' [18].

### 0.10.1 Ratio of Profiles

First, a reference profile was arbitrarily chosen. We took the ratio of the reference profile against the remaining profiles. We then performed cumulative areawise testing. Under the assumption that profiles contained only WN, the null distribution of cumulative areas was generated using the ratio of WN. More specifically, the R package 'advbiwavelet' only supported an autoregressive model of order 1, hence it was made as close to WN as possible by setting the lag1 autocorrelation coefficient as close to zero as possible (0.0000000001). The set of pointwise significance levels used were  $\alpha_{pw} = \{.18, .16, .14, .12, .10, .08, .06, .04, .02\}$ . By default, the length of noise realizations used to create the null was 100, and the number of data points used in the null distribution was 100 as well. Only a single test was performed with  $\alpha_c = 0.01$ .

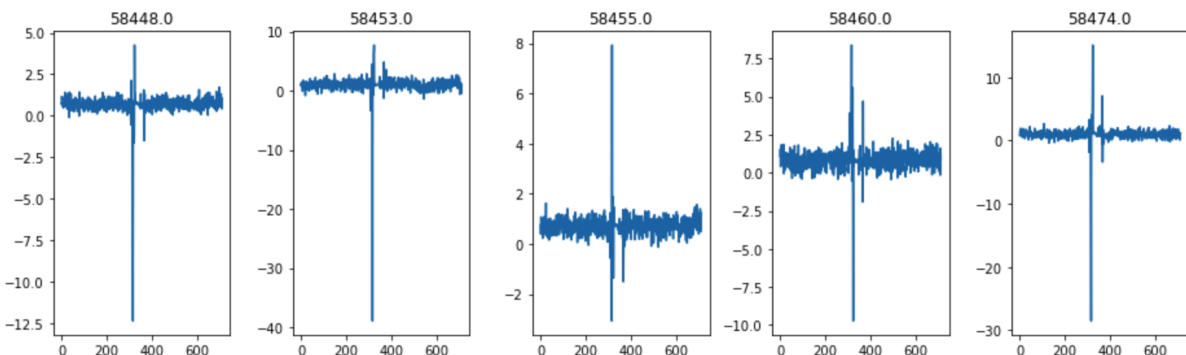


**Figure 36:** Few of the pulse profile ratios.

The test identified a majority of the profiles as significantly different from null profile (when it isn't really visually). This is most likely due to the ratio data itself. As shown above, by the nature of taking ratios, small deviations are exaggerated. This could possibly be fixed by taking ratio of WN with greater standard deviation when calculating null distribution, or maybe not.

### 0.10.2 Difference of Profiles

Using the same reference profile, we now take the difference between the reference profile and the remaining profiles. All assumptions/default are same as the ratio testing except using the difference of WN to produce our null distribution of cumulative areas, and we tested it for three cases:  $\alpha_c = 0.01, 0.05, 0.1$ .

A sanity check we can do is to observe the result for MJD 58453. It was observed that the profile at MJD 58453 is almost identical to our reference profile, as shown below. Ideally, we would expect no significant patches in the spectrum.

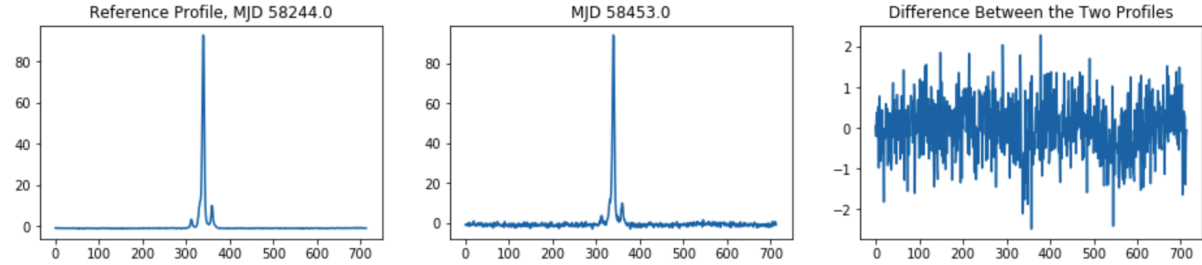


**Figure 37:** (a) Null Profile (b) Profile at MJD 58453 (c) The difference between the two profiles. The two profiles, when overplotted, are almost identical.

As expected, the spectrum at MJD 58453 below shows no significant patches at  $\alpha_c = .01$ . This was not true with the ratio case. However, it does begin producing patches at  $\alpha_c = .05$  and  $\alpha_c = .1$ . The test isn't failing, it is doing its job. As we saw in Figure 37, there are features that aren't due to pure WN. However, visually the profile should be considered normal mode, and we want to ignore these minor features in the difference. Thus, we can conclude it is necessary to have a very strict  $\alpha_c$ .

MJD: 58453,  $\alpha_{\text{cum}}: 0.01$

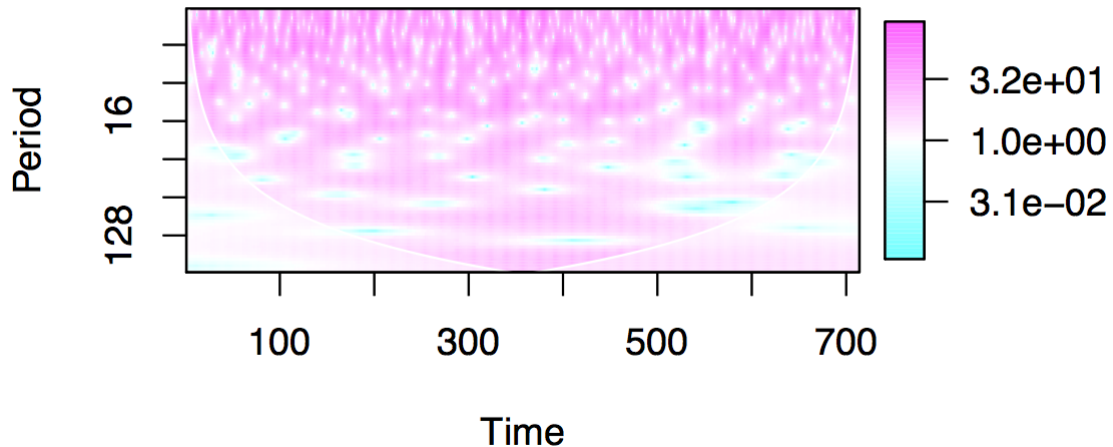


**Figure 38:** Spectrum of difference of MJD 58453 profile at  $\alpha_c = .01$ . No significant patches as expected. [R 'adadvbiwavelet']

MJD: 58453,  $\alpha_{\text{cum}}: 0.05$

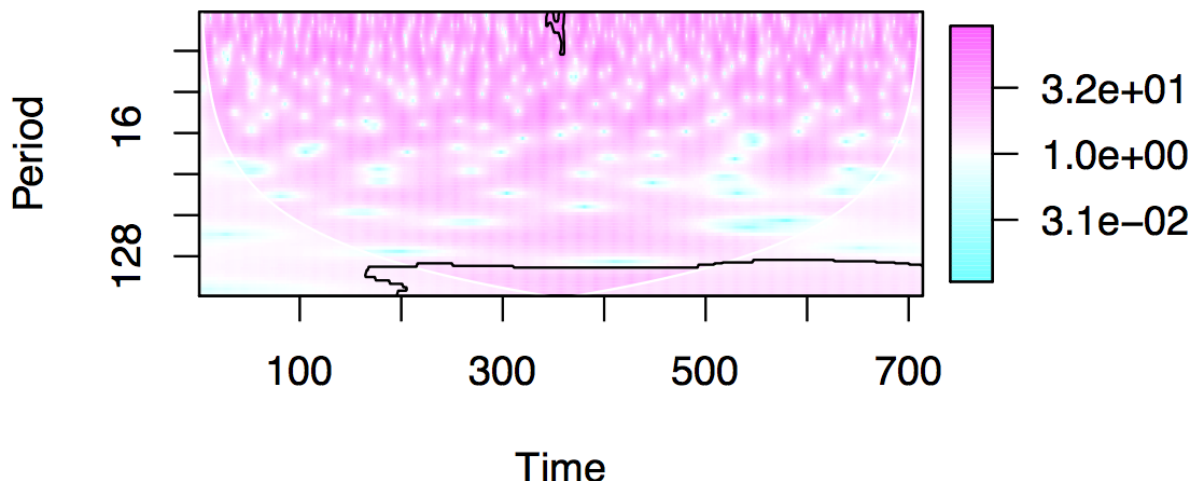


**Figure 39:** Spectrum of difference of MJD 58453 profile at  $\alpha_c = .05$ . Spurious patches begin to appear. [R 'adadvbiwavelet']

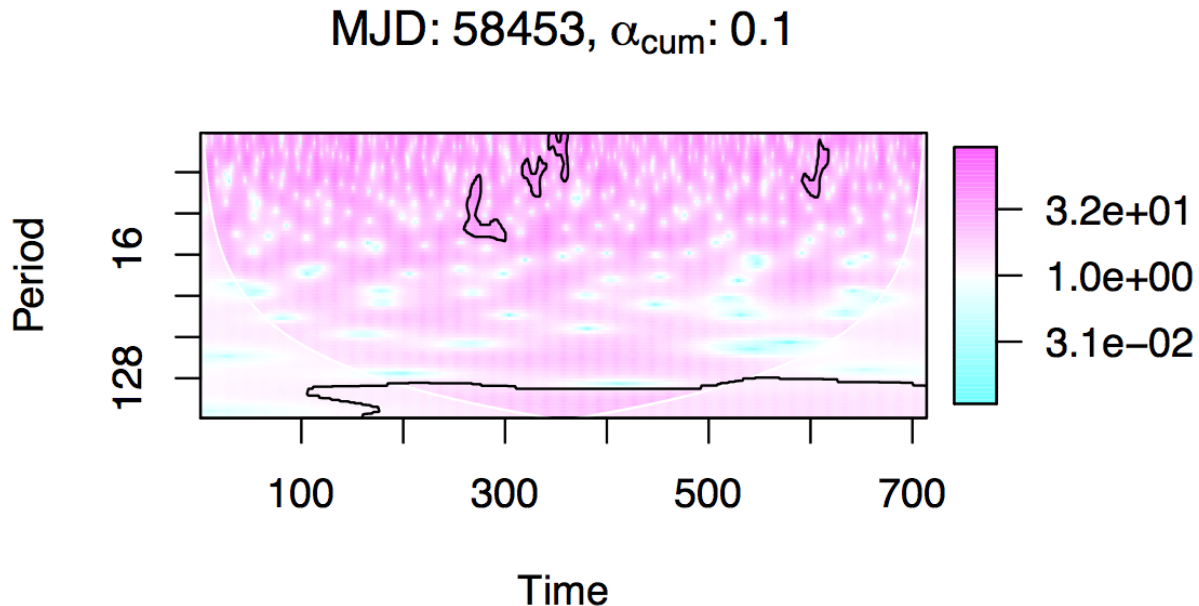


**Figure 40:** Spectrum of difference of MJD 58453 profile at  $\alpha_c = 0.1$ . More spurious patches are born. [R 'advbiwavelet']

Now, what about the other profiles? First, take a look at the differences of profiles. Many of them have several very sharp features on top of white noise.

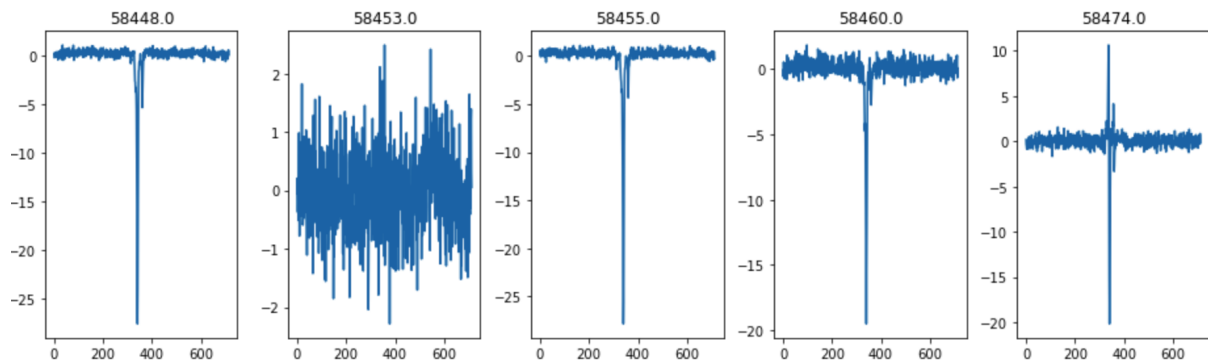


**Figure 41:** Differences in Profiles. MJD 58453 was an exception.

After applying the Morlet wavelet transform and the cumulative areawise test, almost all of the spectra displayed triangular patches with a wide base and stretched top. The typical spectrum is shown below.

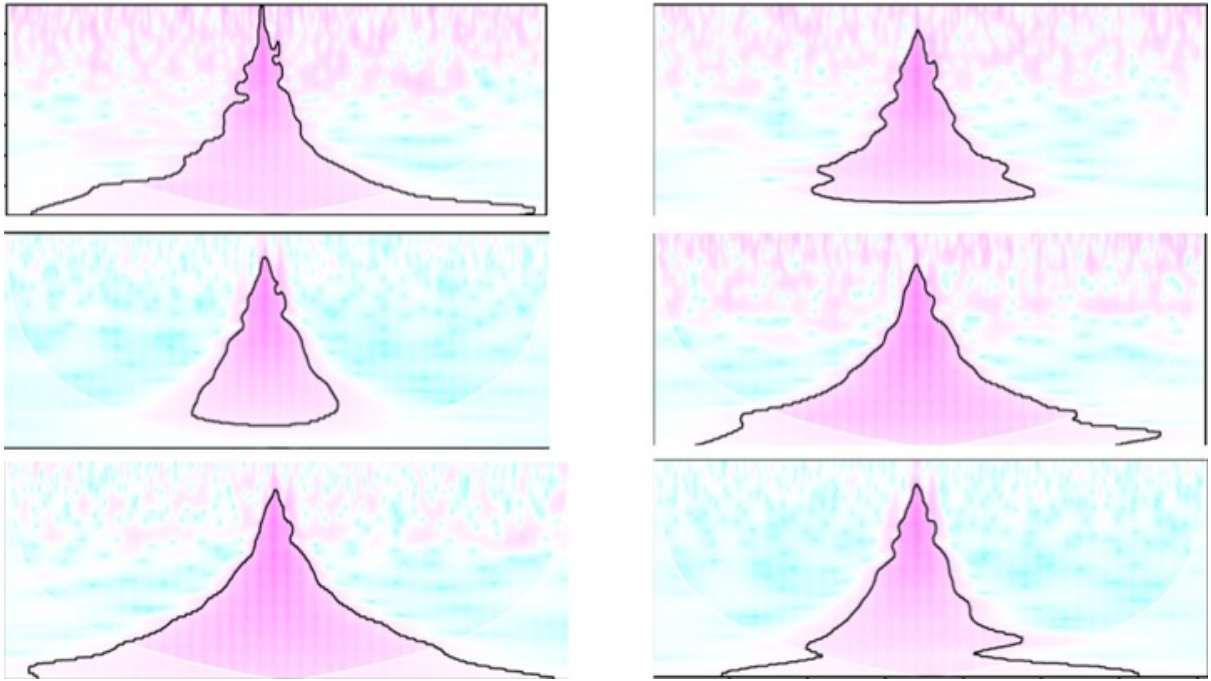
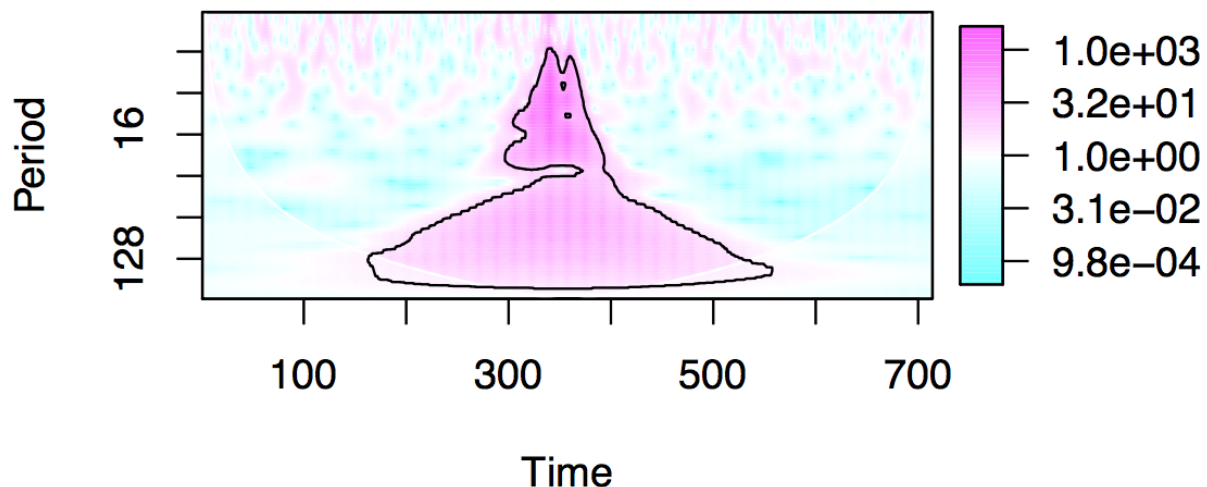


**Figure 42:** Typical spectrum of profile differences at  $\alpha_c = .01$ . They all share some form of triangular patch. [R 'advbwavelet']

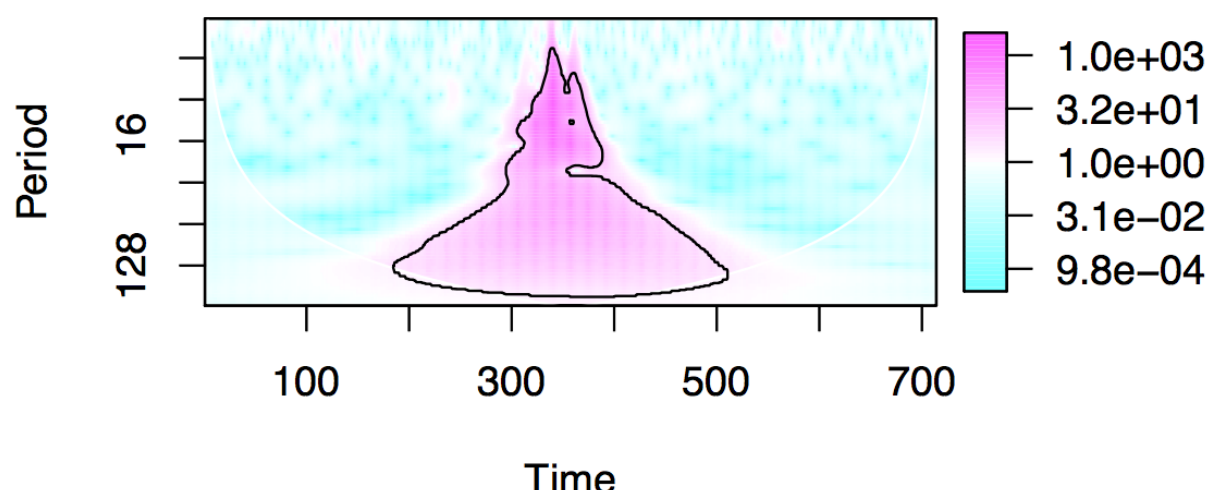
So far, not very promising. Technically, the test is saying almost all the profiles are significant. Like the testing on profile ratios, wavelet spectra don't seem to distinguish modes. However, there is a big difference from the ratio spectra. While the majority of ratio spectra had holes in its patches, that is not the case for difference in profiles. In fact, there are only 11 out of 61 spectra with holes, and another 4 that almost form holes. The numbers are the same for  $\alpha_c = .01, .05, .1$ .

Remembering that holes are often an indication of a significant feature, what happens if we impose a somewhat arbitrary condition that patches must have holes to be significant? It turns out then that 7 out of the 11 spectra with holes identify 7 out of 12 profiles visually classified to have a decrease in the third peak amplitude. Also, 1 out of the 4 spectra that almost form holes identify another 1 out of the 12 as well. The next six figures show the spectra which correctly identified profiles whose third peak decreases in amplitude. The four spectra which almost formed holes are also shown after. All made using R 'advbwavelet' [18].

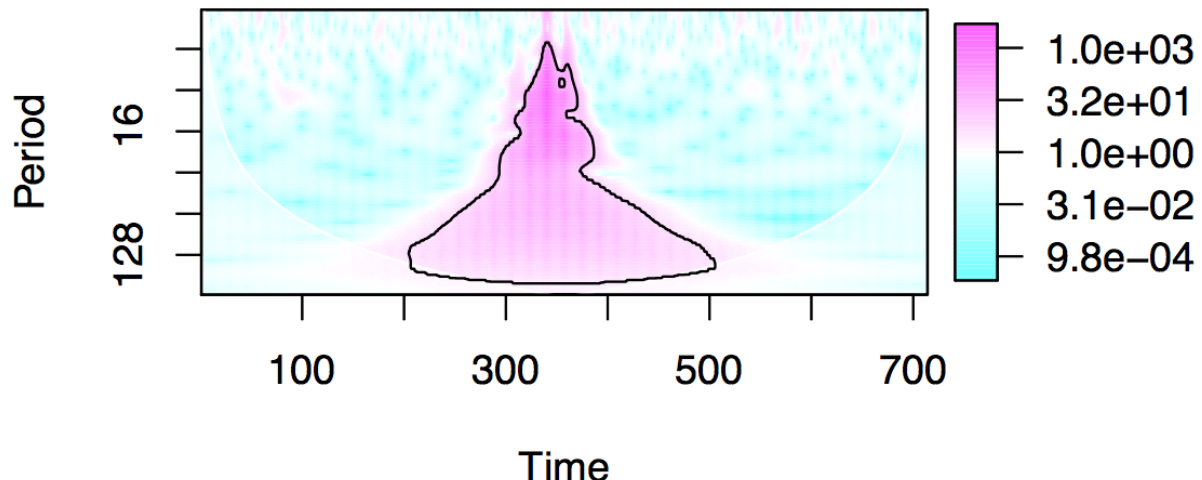
MJD: 58302,  $\alpha_{\text{cum}}$ : 0.01



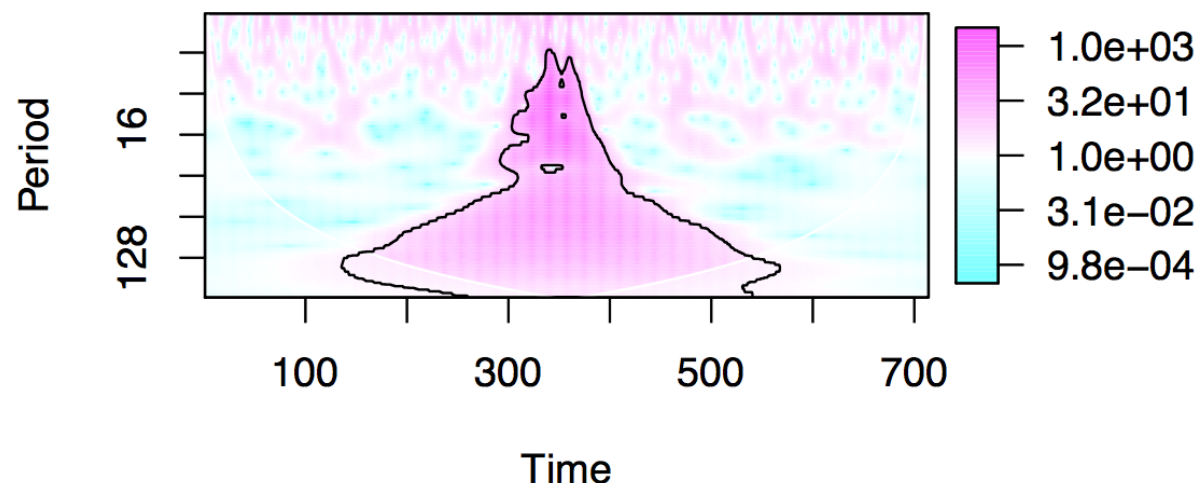
MJD: 58342,  $\alpha_{\text{cum}}$ : 0.01



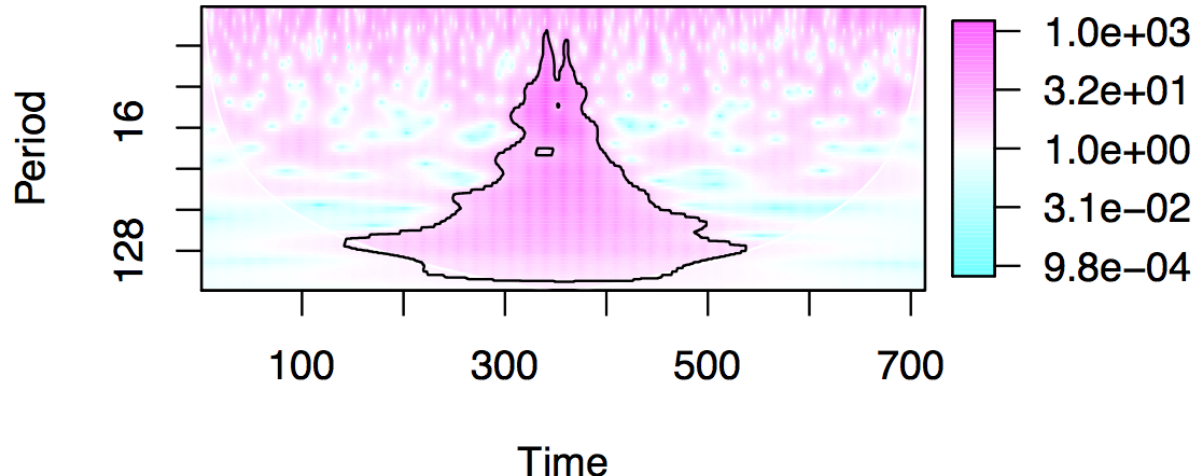
MJD: 58363,  $\alpha_{\text{cum}}$ : 0.01



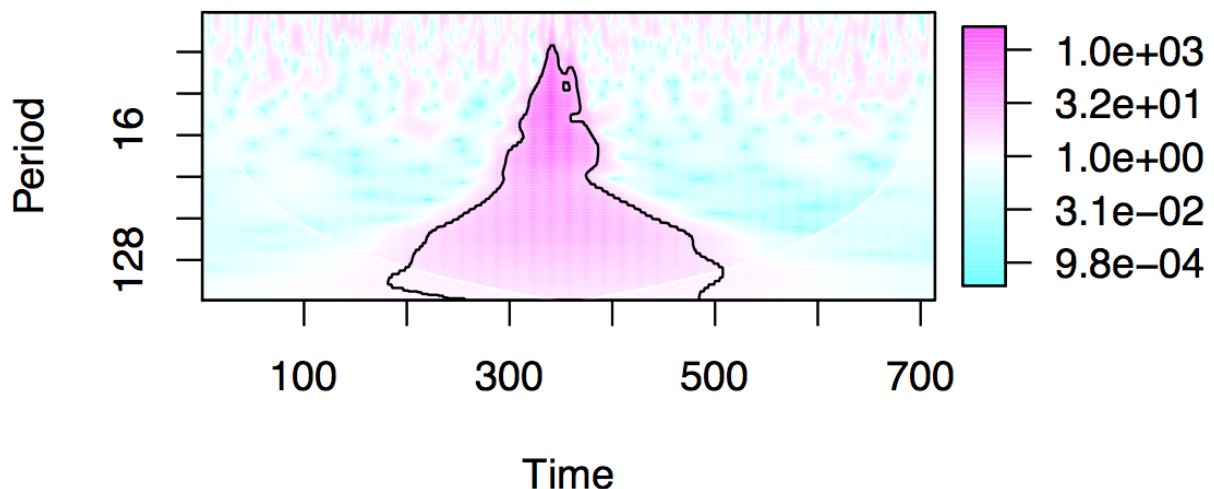
MJD: 58411,  $\alpha_{\text{cum}}$ : 0.01



MJD: 58413,  $\alpha_{\text{cum}}$ : 0.01



MJD: 58632,  $\alpha_{\text{cum}}$ : 0.01



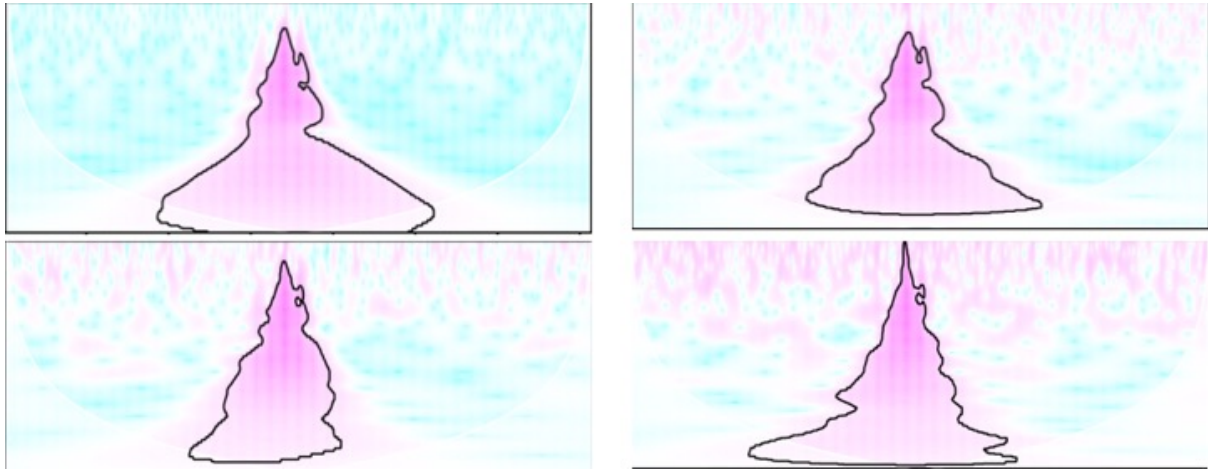


**Figure 43:** Four spectra that almost formed holes. One of them corresponds to a decrease in third peak of profile.

So does a hole indicate a mode change? Maybe, maybe not. Correctly identifying more than 50% of visually abnormal profiles seems like more than a coincidence. However, visually comparing, the other 5 profiles identified as significant don't differ from the null profile much. It's not easy to form a conclusion without fully understanding what sort of features cause holes, and what it means in terms of the difference of profiles.

However, the triangular patch shared by majority of spectra seems to be caused by the sharp Gaussian-like features in the profile differences. As the standard deviation of a Gaussian feature decreases, its significance patch in the timescale domain seems to stretch more sharply along the scale axis, producing a triangle with a wide base and sharp top. Illustrated below.

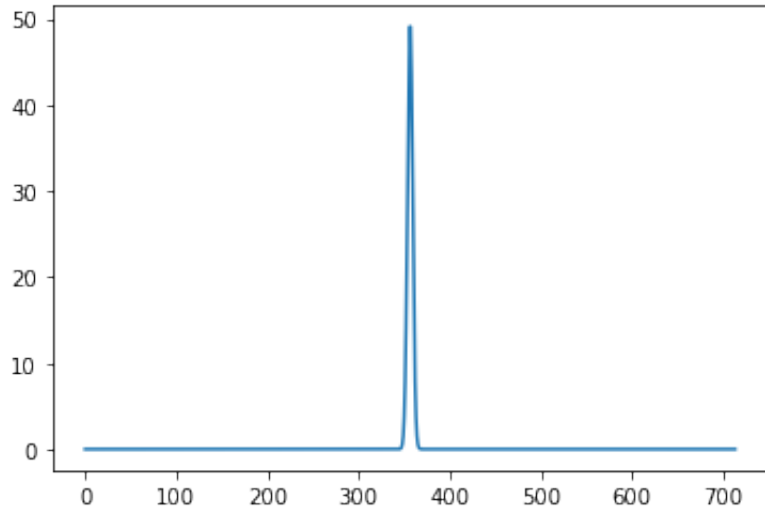


**Figure 44:** A sharp Gaussian feature similar to those commonly seen in profile differences (Figure 41)

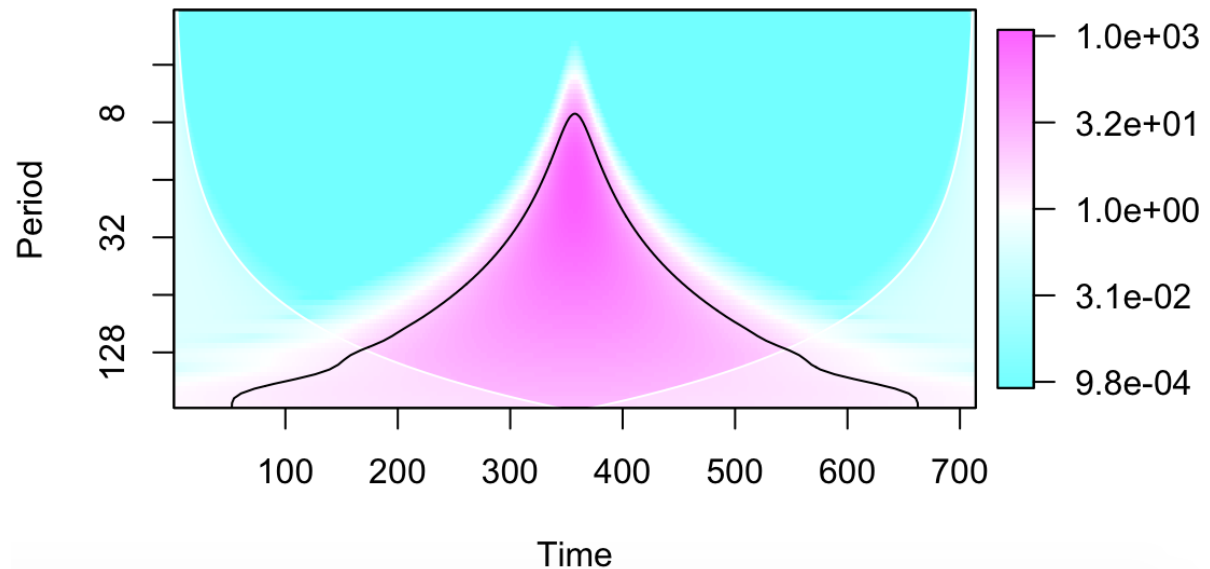


**Figure 45:** The sharp Gaussian's corresponding spectra with  $\alpha_c = 0.01$ . It seems to reproduce the triangle shaped patches seen in the J0332 profile differences. [R 'adadvbiwavelet']

Another question we can ask is, what features in the profile differences cause holes? There may be other, more complex causes, but one explanation is simply that holes are byproducts of several Gaussians nearby each other in the profile differences. This results in the triangular shaped patches "merging" in the timescale plane, as shown below. Spectra produced with R 'adadvbiwavelet'.

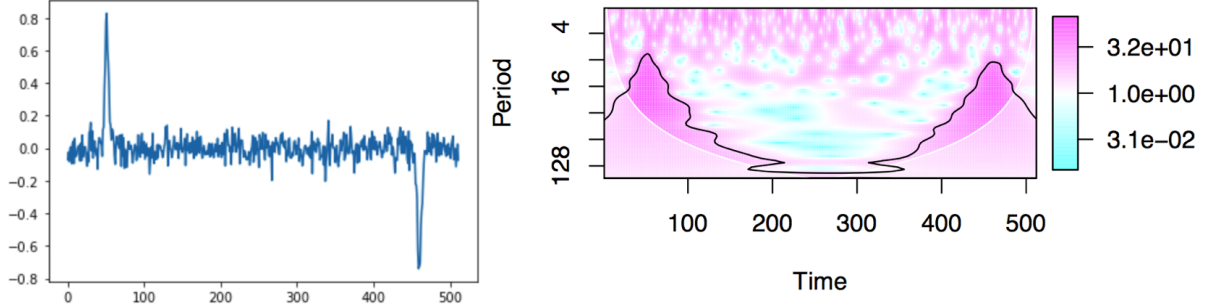


**Figure 46:** Difference between two simulated profiles, with large separation (left). Corresponding spectrum with  $\alpha_c = .05$  (right).

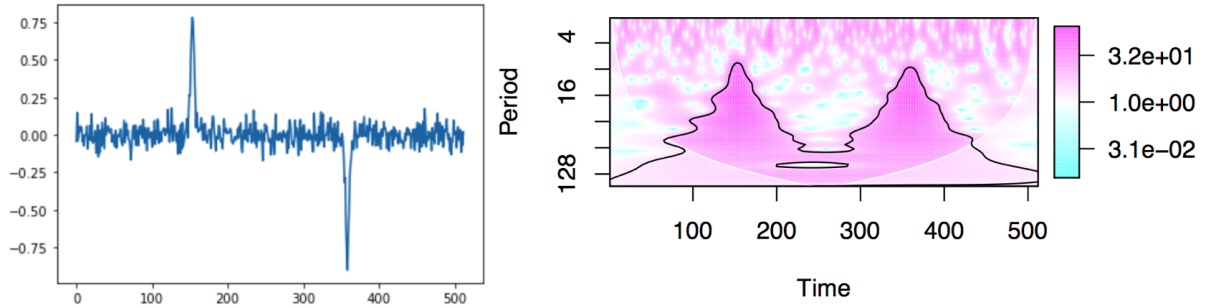


**Figure 47:** Difference between two simulated profiles, with medium separation (left). Corresponding spectrum with  $\alpha_c = .05$  (right).

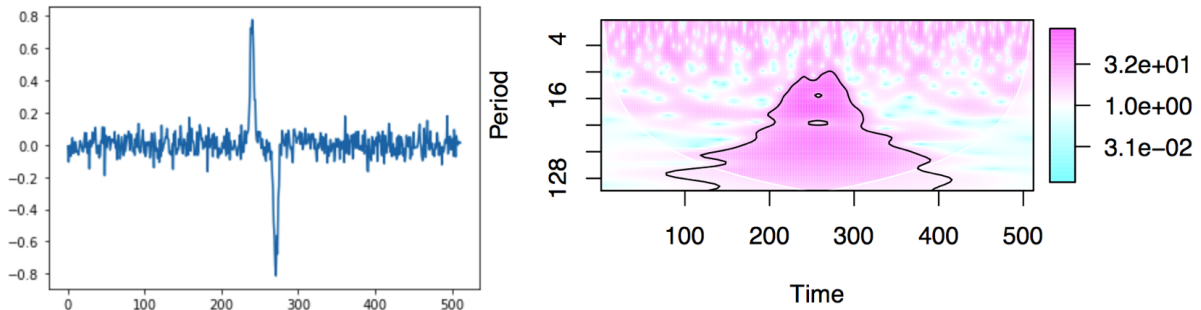


**Figure 48:** Difference between two simulated profiles, with small separation (left). Corresponding spectrum with  $\alpha_c = .05$  (right).

Holes form between two merging patches. A narrower Gaussian feature results in smaller holes higher on the triangle. A wider Gaussian feature results in holes elongated along time, and occurring lower on the triangle. We saw that almost all profile differences

contained only narrow Gaussians, and the holes that did appear were near the top of triangular patches, lending credibility to the idea. However, it does not explain why almost all profile differences contained narrow Gaussians but only 11 of them produced holes, and more than half of them identified a mode change.

It was noticed that the tiniest phase misalignment introduces holes as well, as this produces narrow Gaussian features in the difference.

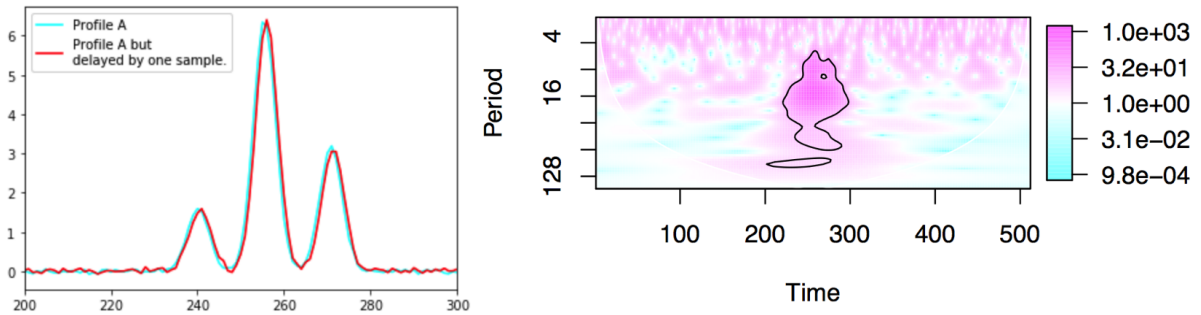


**Figure 49:** A profile but delayed one sample (left), and the spectrum with  $\alpha_c = .05$  (right). [R 'advbiwavelet']

Out of the 11 profiles identified by wavelet analysis (contains holes), one of them seems to have a minor phase misalignment. The plots are shown below.

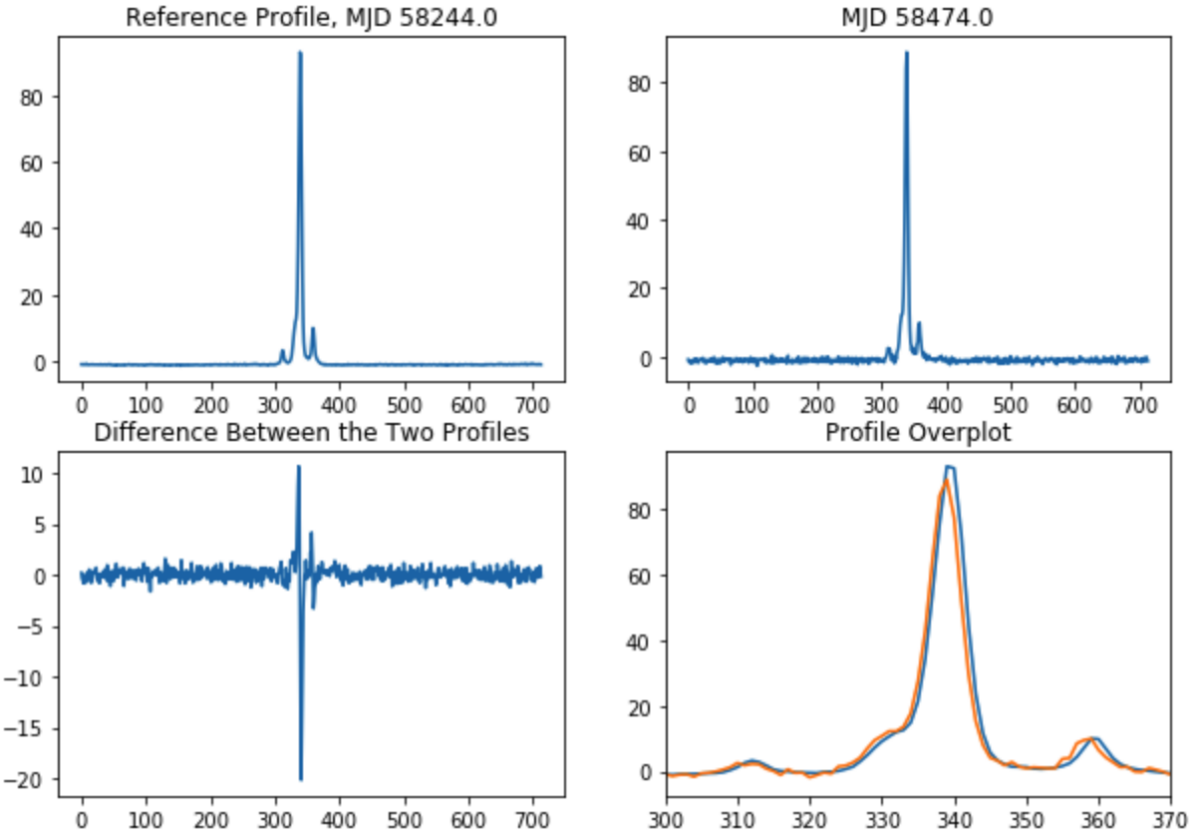


**Figure 50:** A minute phase misalignment may have contributed to a hole in spectrum, giving a false positive.

Again, it's not clear whether holes indicate a mode change, an artificial error, or a mix of both. The interpretation of holes is still not lucid. However, the fact that requiring holes to be considered significant correctly identified mode changes  $\frac{7}{12} \sim 58\%$  of the time is interesting. Also note that we are comparing test results against visually classified mode changes, which looked for changes in amplitude of only the 3rd peak.

A way to improve results might be to think of another form of data to perform wavelet analysis on instead of difference or ratio of profiles. These methods were chosen because the null distribution was being generated from WN, and so the profile data had to be manipulated in a way such that "no mode change" was equivalent to manipulated data exhibiting pure WN. Another way to truly verify test accuracy is simply use a larger dataset.

## 0.11 TEST COMPARISONS

Finally, a comparison of all the tests against visually classified profiles. Visual classification (only considering amplitude decrease in 3rd peak) identified 12 out of 62 profiles as abnormal. KS test identified 3 out of 62, but these three did not match any of those visually identified. As seen in Figure 17, it probably identified large amplitude changes in the central peak, as opposed to the small change in the 3rd peak. Wavelet analysis on the ratio of profiles was not very informative. Wavelet analysis on difference of profiles (with condition that patches must have holes) at  $\alpha_c = .01, .05$ , and  $.1$  all identified the same 11 out of 62 profiles as significant. 7 out of those 11 matched those visually identified. Thus, it had a success rate of  $7/12 = 58\%$ . There were an additional 4 spectra that almost formed holes, and one of them also matched that of visual classification. Figure 51 summarizes all test results.

## Mode Classifications of Different Tests

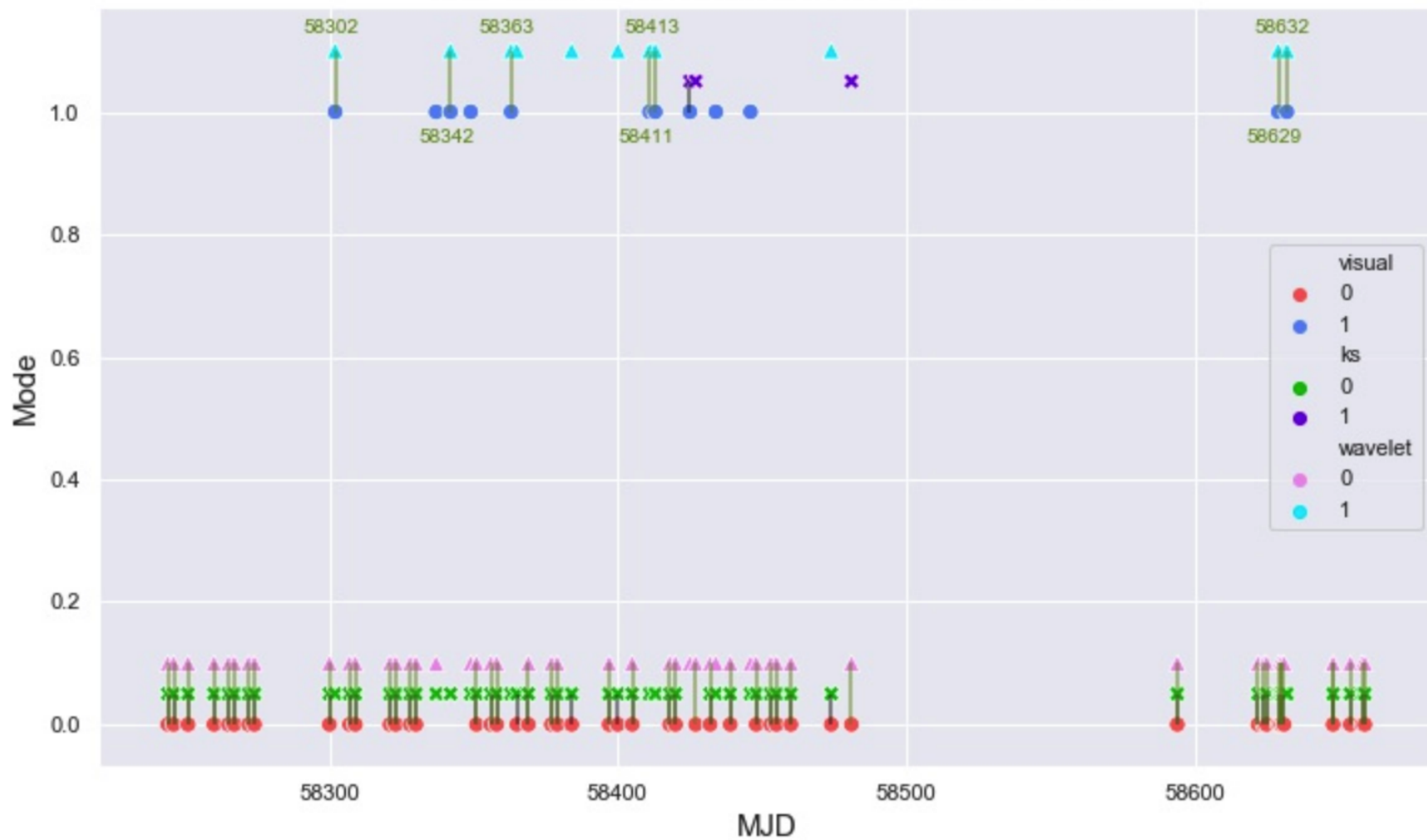


**Figure 51:** Abnormal if mode  $\geq 1$ , normal if not. Circles for visual classifications. **X** for KS test classifications. Triangles for wavelet difference classifications. Black lines where visual and KS test results match. Olive lines where visual and wavelet test results match, with MJDs displayed.

## **0.12 ADDITIONAL RESOURCES**

Main resource for learning wavelet analysis was Introduction to Wavelet Analysis by Walnut [24]. It is a perfect introductory textbook, with interpretations, examples, and plenty of figures. Chapters 1-4 introduce mathematics required to understand wavelet analysis, and may be skipped. Chapters 5 and 6 describe the Haar system and DHT. These two chapters provide a intuition for the more general DWT and MRA in the following sections. Chapter 7 describes MRA, and Chapter 8 describes generalized DWT. Chapter 11, wavelet packets and discrete wavelet packet transform (DWPT), might be of further interest. The Ten Lectures on Wavelets [6] is a bit more math heavy.

Various software were used to create wavelet spectrum plots and perform DWT. They are Python 'PyWavelets' [8], R 'WaveletComp' [1], R 'biwavelet' [20], and R 'advbiwavelet' [18]. 'PyWavelets' has built-in datasets such as El-Nino and ECG signals to play around with. The ECG dataset was used to produce Figure 29. Note about 'advbiwavelet', it is not a package that is published on R-CRAN, but a set of functions designed to be used in conjunction with 'biwavelet'. The package 'advbiwavelet' can be downloaded from Justin Schulte's personal website :

<http://justinschulte.com/wavelets/advbiwavelet.html>

For producing wavelet spectra, I have found the best tool to be R 'biwavelet' and 'advbiwavelet' packages. 'WaveletComp' does have a decent plotting function as well, for its contours only display pointwise significance. 'PyWavelets' does not have a built-in plotting function. Also, MATLAB has a Wavelet Toolbox that is pretty polished and well documented, but I believe it again does not support contours for cumulative areawise/arcwise significance testing.

A summary of development of wavelet significance testing is as follows:  
 Pointwise [23] → Areawise [14] → Geometric and Topological [16] → Cumulative Areawise [17] and Cumulative Arcwise [18]. Cumulative arcwise testing is primarily designed to detect periodicities in a signal.

## 0.13 REFERENCES

- [1] Angi Roesch and Harald Schmidbauer (2018). WaveletComp: Computational Wavelet Analysis. R package version 1.1.  
<https://CRAN.R-project.org/package=WaveletComp>
- [2] "The ATNF Pulsar Database." Australia Telescope National Facility,  
[www.atnf.csiro.au/research/pulsar/psrcat/](http://www.atnf.csiro.au/research/pulsar/psrcat/).
- [3] Burke, Bernard F., and Francis Graham-Smith. An Introduction to Radio Astronomy. Cambridge University Press, 1997.
- [4] Cocuzzo, Daniel, et al. "In Vivo Brain Magnetic Resonance Spectroscopy: A Measurement of Biomarker Sensitivity to Post-Processing Algorithms." IEEE Journal of Translational Engineering in Health and Medicine, vol. 2, 2014, pp. 1-17., doi:10.1109/jtehm.2014.2309333.
- [5] "Continuous Wavelet Transform (CWT)." Weisang.com,  
[www.weisang.com/en/documentation/timefreqspectrumanalgorithmscwt\\_en/](http://www.weisang.com/en/documentation/timefreqspectrumanalgorithmscwt_en/).
- [6] Daubechies, Ingrid. Ten Lectures on Wavelets. Society for Industrial and Applied Mathematics, 1992.
- [7] Eppstein, David, and Michael T. Goodrich. "Succinct Greedy Geometric Routing Using Hyperbolic Geometry." IEEE Transactions on Computers, vol. 60, no. 11, 2011, pp. 1571-1580., doi:10.1109/tc.2010.257.
- [8] Gregory R. Lee, Ralf Gommers, Filip Wasilewski, Kai Wohlfahrt, Aaron OâŽLeary (2019). PyWavelets: A Python package for wavelet analysis. Journal of Open Source Software, 4(36), 1237, <https://doi.org/10.21105/joss.01237>.
- [9] Hopkins, Rosemary Lorena. "ENG4BF3 Medical Image Processing." SlidePlayer, 2015, [slideplayer.com/slide/6077448](http://slideplayer.com/slide/6077448).
- [10] Kimpson, Tom. âIJGBT Visit.â Tom Kimpson, 18 May 2017, [tomkimpson.com/observation/GBT/](http://tomkimpson.com/observation/GBT/).
- [11] "Kolmogorov-Smirnov Test." Wikipedia, Wikimedia Foundation, 11 Aug. 2019, [en.wikipedia.org/wiki/Kolmogorov%E2%80%93Smirnov\\_test](https://en.wikipedia.org/wiki/Kolmogorov%E2%80%93Smirnov_test).
- [12] Lorimer, Duncan Ross, and Michael Kramer. Handbook of Pulsar Astronomy. University Press, 2012.
- [13] Lyne, A. G., and Francis Graham Smith. Pulsar Astronomy. Cambridge University Press, 2012.
- [14] Maraun, D., et al. "Nonstationary Gaussian Processes in Wavelet Domain: Synthesis, Estimation, and Significance Testing." Physical Review E, vol. 75, no. 1, 2007,

doi:10.1103/physreve.75.016707.

- [15] Observer. "Giant Metrewave Radio Telescope (GMRT) Home Page." Giant Metrewave Radio Telescope (GMRT) Home Page, [www.gmrt.ncra.tifr.res.in/](http://www.gmrt.ncra.tifr.res.in/).
- [16] Schulte, J. A., et al. "Geometric and Topological Approaches to Significance Testing in Wavelet Analysis." *Nonlinear Processes in Geophysics*, vol. 22, no. 2, 2015, pp. 139-156., doi:10.5194/npg-22-139-2015.
- [17] Schulte, Justin A. "Cumulative Areawise Testing in Wavelet Analysis and Its Application to Geophysical Time Series." *Nonlinear Processes in Geophysics*, vol. 23, no. 1, 2016, pp. 45-57., doi:10.5194/npg-23-45-2016.
- [18] Schulte, Justin A. "Statistical Hypothesis Testing in Wavelet Analysis: Theoretical Developments and Applications to Indian Rainfall." *Nonlinear Processes in Geophysics*, vol. 26, no. 2, 2019, pp. 91-108., doi:10.5194/npg-26-91-2019.
- [19] Smith, Julius O. *Mathematics of the Discrete Fourier Transform (DFT): with Audio Applications*. BookSurge, 2010.
- [20] Tarik C. Gouhier, Aslak Grinsted, Viliam Simko (2019). R package biwavelet: Conduct Univariate and Bivariate Wavelet Analyses (Version 0.20.19). Available from <https://github.com/tgouhier/biwavelet>
- [21] Taylor, J H. "Pulsar Timing and Relativistic Gravity." *Classical and Quantum Gravity*, vol. 10, no. S, 1993, doi:10.1088/0264-9381/10/s/017.
- [22] Taylorb., Arnold, and Emerson Johnw. "Nonparametric Goodness-of-Fit Tests for Discrete Null Distributions." *The R Journal*, vol. 3, no. 2, 2011, p. 34., doi:10.32614/rj-2011-016.
- [23] Torrence, C. and Compo, G. P.: *A Practical Guide to Wavelet Analysis*, Bull. Am. Meteorol. Soc., 79, 61–78, 1998.
- [24] Walnut, David F. *An Introduction to Wavelet Analysis*. Birkhauser, 2004.